Determination of optimal shot peen forming patterns using the theory of non-Euclidean plates

Vladislav Sushitskii
PhD Student
Laboratory of Multiscale Mechanics (LM2)
Aluminium Research Center (REGAL)
Polytechnique Montreal
Montreal, QC H3T1J4
Canada
Email: vladislav.sushitskii@polymtl.ca

Wim M. van Rees
Assistant Professor
Department of Mechanical Engineering
Massachusetts Institute of Technology
Cambridge, MA 02139-4307
Email: wvanrees@mit.edu

Martin Levesque
Professor
Laboratory of Multiscale Mechanics (LM2)
Polytechnique Montreal
Montreal, QC H3T1J4
Canada
Email: martin.levesque@polymtl.ca

Frederick P. Gosselin
Associate Professor
Laboratory of Multiscale Mechanics (LM2)
Aluminium Research Center (REGAL)
Polytechnique Montreal
Montreal, QC H3T1J4
Canada
Email: frederick.gosselin@polymtl.ca

ABSTRACT

We show how a theoretical framework developed for modelling nonuniform growth can model the shot peen forming process. Shot peen forming consists in bombarding a metal panel with multiple millimeter-sized shot, that induce local bending of the panel. When applied to different areas of the panel, peen forming generates compound curvature profiles starting from a flat state. We present a theoretical approach and its practical realization for simulating peen forming numerically. To achieve this, we represent the panel undergoing peen forming as a bilayer plate, and we apply a geometry-based theory of non-Euclidean plates to describe its reconfiguration. Our programming code based on this approach solves two types of problems: it simulates the effect of a predefined treatment (the forward problem) and it finds the optimal treatment to achieve a predefined target shape (the inverse problem). Both problems admit using multiple peening regimes simultaneously. The algorithm was tested numerically on 200 randomly generated testcases.

NOMENCLATURE

A_c	Current local area
A_{tar}	Target local area
A_{total}	Total area of the plate in its initial configuration
$\mathbf{a}$	2×2 matrix defining the local first fundamental form
$(\mathbf{a}_{r,t}, \mathbf{a}_{r,b})$	Two first fundamental forms defining the bilayer rest configuration
$(\mathbf{a}_{r,t}^{ortho}, \mathbf{a}_{r,b}^{ortho})$	Two first fundamental forms defining the bilayer rest configuration for the case of local in-plane orthotropic growth
$(\mathbf{a}_{r,t}^{new}, \mathbf{a}_{r,b}^{new})$	Two first fundamental forms defining the adjusted bilayer rest configuration
$(\mathbf{a}_{rf,t}, \mathbf{a}_{rf,b})$	Two first fundamental forms defining the bilayer rest configuration obtained on the final iteration
$\mathbf{b}$	2×2 matrix defining the local second fundamental form
$(\mathbf{a}_c, \mathbf{b}_c)$	The first and the second fundamental forms defining the monolayer current con-

	figuration
$(\mathbf{a}_c^{new}, \mathbf{b}_c^{new})$	The first and the second fundamental forms defining the monolayer current configuration, which was obtained by assignment of the adjusted rest configuration and subsequent deformation
$(\mathbf{a}_f, \mathbf{b}_f)$	The first and the second fundamental forms defining the monolayer final configuration
$(\mathbf{a}_{init}, \mathbf{b}_{init})$	The first and the second fundamental forms defining the monolayer initial configuration
$(\mathbf{a}_r, \mathbf{b}_r)$	The first and the second fundamental forms defining the monolayer rest configuration
$(\mathbf{a}_r^{new}, \mathbf{b}_r^{new})$	The first and the second fundamental forms defining the adjusted monolayer rest configuration
$(\mathbf{a}_r^{ortho}, \mathbf{b}_r^{ortho})$	The first and the second fundamental forms defining the monolayer rest configuration for the case of local in-plane orthotropic growth
$(\mathbf{a}_{tar}, \mathbf{b}_{tar})$	The first and the second fundamental forms defining the monolayer target configuration
$\mathcal{C}_c$	Point cloud describing the current configuration
$\mathcal{C}_c^{new}$	Point cloud describing the current configuration obtained by assignment of the adjusted rest configuration and subsequent deformation
$\mathcal{C}_f$	Point cloud describing the final configuration
$\mathcal{C}_{tar}$	Point cloud describing the target configuration
d_H	The Hausdorff distance
E_{BL}	Elastic energy of a bilayer
E_{ML}	Elastic energy of a monolayer
$\vec{e}_0$, $\vec{e}_1$, $\vec{e}_2$	Edge vectors defining three edges of a triangular element
H_c	Current local mean curvature
H_{tar}	Target local mean curvature
h	The plate thickness

$\mathbf{I}$	The identity matrix
K	Number of triangular elements in the model
k_A	Ratio between the target local area and the current local area
k_H	Ratio between the target local mean curvature and the current local mean curvature
M	Maximal number of iterations
N	Number of predefined peening regimes
$\vec{m}$	Mapping defining position of each point of the mid-surface in $\mathbb{R}^3$ based on its coordinates in U
$\vec{n}$	Unit normal vector
$\vec{n}_0$, $\vec{n}_1$, $\vec{n}_2$	Edge-directors defining normals to the three edges of a triangular element
$\vec{r}$	Radius-vector defining position of each point of the plate in space
$\mathbf{S}$	The shape operator
$\mathbf{S}_c$	Current shape operator
$\mathbf{S}_r$	Rest shape operator
$\mathbf{S}_r^{new}$	Adjusted rest shape operator
$\mathbf{S}_{tar}$	Target shape operator
U	Domain of $\mathbb{R}^2$ englobing the plate mid-surface in coordinates (x, y)
U_1	Sub-domain of U
$\vec{v}_0$, $\vec{v}_1$, $\vec{v}_2$	Position vectors defining three vertices of a triangular element
(x, y)	Lagrangian curvilinear coordinates parametrizing the plate mid-surface
Y	Young modulus
z	The through-thickness coordinate
Γ	Total eigenstrain
Γ_1	The first eigenstrain moment
δ	The upper threshold for $\lvert k_H \rvert$
$\boldsymbol{\varepsilon}$	Eigenstrain tensor induced by the peening treatment
$\boldsymbol{\varepsilon}^{el}$	Strain tensor reflecting the elastic material response

$\boldsymbol{\varepsilon}^{res}$	Residual strain tensor
$(\varepsilon^t, \varepsilon^b)$	Eigenstrain induced in the top and bottom layers of a bilayer respectively
$(\varepsilon^t_{avg}, \varepsilon^b_{avg})$	The average of the orthotropic eigenstrain in two principal directions on the top and bottom layers respectively
$(\varepsilon^{cen,t}, \varepsilon^{cen,b})$	A group centroid on the plane $(\varepsilon^t, \varepsilon^b)$
$(\varepsilon^{rf,t}, \varepsilon^{rf,b})$	Eigenstrain prescribed to the top and bottom layers by $(\mathbf{a}_{rf,t}\,, \mathbf{a}_{rf,b})$
(θ^t, θ^b)	Angles between the local principal strain direction and the x axis on the top and bottom layers respectively
ν	Poisson's ratio
τ	Threshold for the dimensionless error between the current and the target configurations used as a stop condition
φ_0, φ_1, φ_2	Angles of inclination of the edge-director vectors $\vec{n}_0$, $\vec{n}_1$, $\vec{n}_2$ with respect to the average of the adjacent face normals
Ω	Dimensionless error between the final and the target configurations

INTRODUCTION

Shot peen forming is a cost-effective technology for shaping large metal plates, such as airplane wing skins, without dies. It consists in bombarding the surface of a component with a large number of millimeter sized shot made of steel, glass or ceramic. The velocity of a shot is sufficiently high to plastically deform the upper layer of the plate upon impact and to stretch the plate locally. This effect causes local bending of thin components and leads to a convex curvature on the peened side [1]. Repeated impacts also induce a field of compressive residual stress, that can improve fatigue life [2].

When developping a shot peen forming process, one is faced with two types of problems as schematized in Fig. 1: *the forward problem* and *the inverse problem* [3]. The forward problem is formulated with the following question: which shape will the component adopt if it is peened according to a given pattern? The inverse problem denotes the following: given an initial shape of the component and the target shape, how should one peen the component to make it deform into the

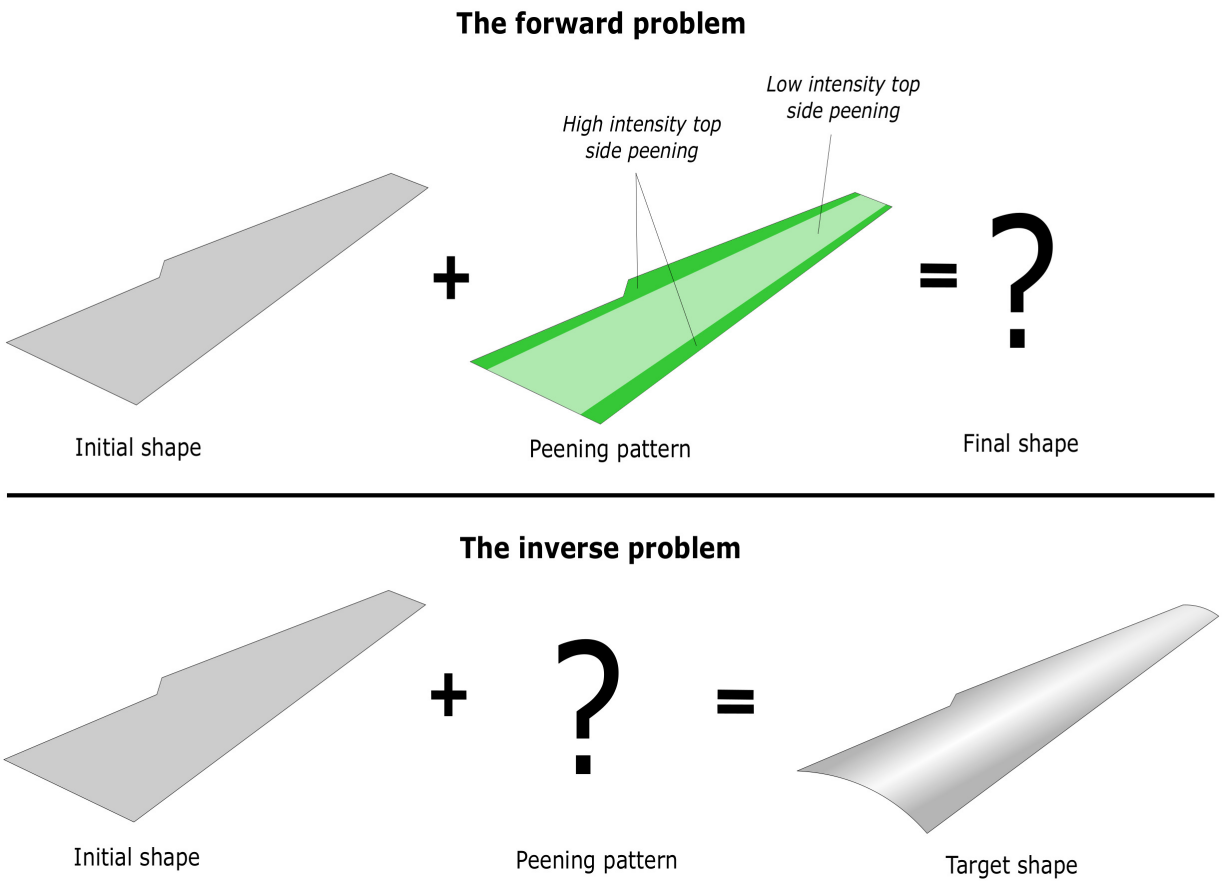

Fig. 1. The two problems of the shot peen forming simulation. a) The forward problem consists in the determination of the final shape of the component given its initial shape and the peening pattern. b) The inverse problem consists in determination of the optimal peening pattern given the initial shape of the component and its target shape.

target shape? A numerical solver for both problems is necessary to optimize the forming process. Thus, without numerical resolution of the inverse problem, the design of a peen forming procedure for each new component is a craft trial-and-error process plagued with risk and uncertainty. It lasts up to several months and implies many scrapped parts. On the other hand, numerical resolution of the forward problem is necessary to check the quality of the inverse problem resolution and to simulate the effect of additional treatments.

A straightforward simulation of individual peening impact, such as the one conducted in [4], is precise but computationally expensive. For this reason, simplified multiscale simulation approaches, such as the *eigenstrain* approach, were developed. It implies formulating the applied peening loads in terms non-elastic strains imposed on the component [5] [6]. The eigenstrain

approach represents the treated plate as a thin bilayer where each layer undergoes a nonuniform plastic in-plane swelling or shrinking. The forward problem in this formulation can be numerically solved using shell finite element models [7] [8]. In addition, such models allow to implement an inverse problem resolution algorithm based on the topology optimization methods [9] [10]. A similar inverse problem resolution approach was also applied in [11] in the context of the *laser* peen forming process. Given that this method is based on numerical optimization, its speed decreases with the number of elements in the model. On the other hand, the inverse problem can be solved using an artificial neural network [8]. The neural network provides near-perfect accuracy and fast calculation on-line. However, it requires the generation of a large finite-element forward problem solution database and a long training phase for each new plate geometry.

To overcome these issues during the inverse problem resolution, we turned to the theory of non-Euclidean plates [12] [13]. This theoretical framework lies at the intersection of mechanics and differential geometry. It precisely describes distortion of multilayer plates induced by the prescription of a nonuniform non-elastic strain. Prescription of such strain makes the surface metric non-Euclidean so that it does not satisfy the compatibility conditions of the Euclidean space, which gives name to the theory [13]. Experiments conducted in the field of 4D printing with elastic polymer sheets have proven the accuracy of the theory of non-Euclidean plates in numerical forward problem resolution. Thus, this theory precisely predicted curvature of spherical, cylindrical and saddle shapes grown out of a flat state by induction of a nonuniform plastic strain [14] [15]. Numerical simulation of growth for these three cases also showed good accordance with analytical shapes [16]. Moreover, this theory predicted the form of more complex shapes, such as helicoid, catenoid or an orchid flower grown out of a flat state using polymer bilayers with oriented filaments [17]. The theory of non-Euclidean plates also provides instruments for an efficient inverse problem resolution. Such algorithms for the case of polymers with oriented local growth are reported in [17] and [18].

In this paper we propose to use the eigenstrain approach to represent the treated plate as a bilayer, and we resort to the theory of non-Euclidean plates to calculate the resulting distortion of the bilayer. To numerically solve the inverse problem, we created an iterative algorithm that implies

resolving the forward problem on each iteration. The algorithm adjusts the peening pattern based on the discrepancy between the current shape, i.e., the shape obtained with the current pattern, and the target shape. The adjustment is done on a local scale using simple arithmetic operations, so the computation speed on this stage stays constant with an increasing number of variables. This stage does not require any preliminary training phase either. The algorithm constitutes a general approach for the inverse problem resolution in case of bilayers subjected to isotropic, i.e. non-oriented, local growth, such as those examined in [15]. When the iterative adjustment is finished, we group the peening pattern to make it practically applicable. In other words, we divide the pattern into zones treated with constant peening regimes. The number of available peening regimes and their intensities are pre-determined based on the practical constraints.

We start this paper with the theoretical background section. First, we examine the eigenstrain approach that relates peen formed plates and swelling non-Euclidean bilayers. Next, we move to the theory of non-Euclidean plates, namely to the geometrical shape description and the forward problem resolution method that it implies. In this section we also formulate the inverse problem in terms of the theory of non-Euclidean plates. We then pass to the methodology section by presenting our inverse problem resolution algorithm and an approach for its numerical implementation. The grouping and validation strategies are presented in the same section. The results of the validation campaign are presented subsequently, and finally the advantages and limitations of our approach are discussed.

THEORETICAL BACKGROUND

The eigenstrain approach and strain decomposition

The term eigenstrains denotes all non-elastic strains arising in the material, such as plastic, thermal or piezoelectric strains [5]. The only type of eigenstrain generated by peen forming is the plastic strain. Indeed, numerous overlapping impact indentations plastically stretch the outer layer of material, and the rest of the material responds to this newly-introduced eigenstrain with the emergence of stress. In order to conserve its integrity and to balance the stress, the plate deforms elastically. In case of small strains the residual strain tensor ε^{res} is additively decomposed into the

eigenstrain part $\boldsymbol{\varepsilon}$ and the elastic part $\boldsymbol{\varepsilon}^{el}$ ([19], Appendix):

$$\boldsymbol{\varepsilon}^{res} = \boldsymbol{\varepsilon} + \boldsymbol{\varepsilon}^{el}. \tag{1}$$

This relation holds for peen forming because the process deals with thin plates and the peening-induced strains are small [4]. The elastic strain may affect the whole plate, while the eigenstrain is present only in the stretched outer layer. The thickness of the plastically deformed outer layer varies depending on the peening parameters and the treated material. With the eigenstrain approach, the resolution of the forward problem for shot peen forming consists in introducing the eigenstrain over the whole shot peened area and determining the elastic springback.

The through-thickness eigenstrain profile

We endow the mid-surface of the plate with two Lagrangian coordinates (x, y), and we assign a Lagrangian coordinate z in the through-thickness direction. The Lagrangian coordinates follow the plate as it deforms. We assume that the material is plastically isotropic, so the eigenstrains are the same in all in-plane directions: $\varepsilon_{xx}(x, y, z) = \varepsilon_{yy}(x, y, z)$. Also, $\varepsilon_{zz} = -2\varepsilon_{xx}$ due to plastic incompressibility. For a small area around a point (x_0, y_0) on the mid-surface, the through-thickness eigenstrain profile $\varepsilon_{xx}(x_0, y_0, z) = \varepsilon_{yy}(x_0, y_0, z)$ can be measured directly using the X-ray diffraction method [20]. Otherwise, it can be deduced from the residual stress profile, which is determined with such methods as hole drilling [21], layer-removal [21] [22] or the two cut compliance method [23]. In this case, the through-thickness eigenstrain profile is reconstructed numerically from the measured residual stress profile [7] [24].

Mechanically, the introduction of the eigenstrain can be modeled as slicing the plate into thin layers, stretching the outer layers separately following the eigenstrain profile, and then gluing everything back. To numerically simplify the problem, we virtually idealize the eigenstrain profile by assuming that the plate consists of two layers of equal thickness that can separately undergo nonuniform in-plane swelling or shrinking. The idealized eigenstrain profile leads to the same

deformed shape as the real one. Figure 2 illustrates both profiles induced on a uniformly treated plate. Mathematically, the idealization procedure consists in finding the local eigenstrain $\varepsilon^t(x,y)$ to be introduced in the top layer and the local eigenstrain $\varepsilon^b(x,y)$ to be introduced in the bottom layer. It is done by equating the total eigenstrain $\Gamma(x,y)$ and the first eigenstrain moment $\Gamma_1(x,y)$ induced locally by the real eigenstrain profile to those induced locally by $\varepsilon^t(x,y)$ and $\varepsilon^b(x,y)$ [7]. In the general case, Γ and Γ_1 are defined as:

$$\Gamma\left(x,y\right) = \int_{-h/2}^{h/2} \varepsilon_{xx}(x,y,z)dz, \tag{2}$$

$$\Gamma_1\left(x,y\right) = \int_{-h/2}^{h/2} \varepsilon_{xx}(x,y,z)zdz, \tag{3}$$

where h stands for the plate thickness. For the idealized bilayer profile Γ and Γ_1 are expressed as:

$$\Gamma\left(x,y\right) = \frac{h}{2}\left(\varepsilon^t\left(x,y\right) + \varepsilon^b\left(x,y\right)\right), \tag{4}$$

$$\Gamma_1\left(x,y\right) = \frac{h^2}{8}\left(\varepsilon^t\left(x,y\right) - \varepsilon^b\left(x,y\right)\right). \tag{5}$$

The idealized eigenstrain is positive on the side that undergoes the peening treatment and is negative on the other side. It should be noted that although ε^t and ε^b give rise to the same

in-plane extension and curvature as the real eigenstrain profile, the idealized one generates a different residual stress profile.

The theory of non-Euclidean plates applied to the modeling of shot peen forming

The theory of non-Euclidean plates allows to numerically determine the elastic response of thin bodies to an applied nonuniform non-elastic strain, e.g., biological growth or eigenstrain. The introduction of such strain leads to the emergence of stresses, which are *entirely* eliminated only if the plate adopts a so-called *rest configuration.* The rest configuration implies $\boldsymbol{\varepsilon}^{res} = \boldsymbol{\varepsilon}$, so it is generally not realizable without the loss of integrity. Instead of the rest configuration the plate adopts an integral *final configuration (final shape)*, which is still residually stressed. The theory of non-Euclidean plates relates the rest and the final configurations through elastic energy and uses tools from differential geometry to describe the shape of plates. We adopted the approach described in [19] for its numerical implementation.

Geometrical shape description

In the framework of the theory of non-Euclidean plates, the plate shape is associated with the shape of its mid-surface [19]. We denote by U the domain of the plane containing the coordinates (x, y) that parametrize the mid-surface: $(x, y) \in U \subset \mathbb{R}^2$. The position of each point of the mid-surface in a 3D space is defined by the mapping $\vec{m} : U \to \mathbb{R}^3$. We adopt the Kirchhoff-Love assumptions, so the position $\vec{r}$ of a point belonging to the plate is expressed as:

$$\vec{r}(x, y, z) = \vec{m}(x, y) + z\vec{n}(x, y), \tag{6}$$

where $\vec{n}$ is the unit normal vector. The mid-surface shape is described by *the first and the second fundamental forms*, that are binary quadratic forms associated with a symmetric 2×2 matrix. Both fundamental forms are local quantities varying smoothly along the surface. The first fundamental form describes changes in the length of curves and areas of regions on the surface. In other

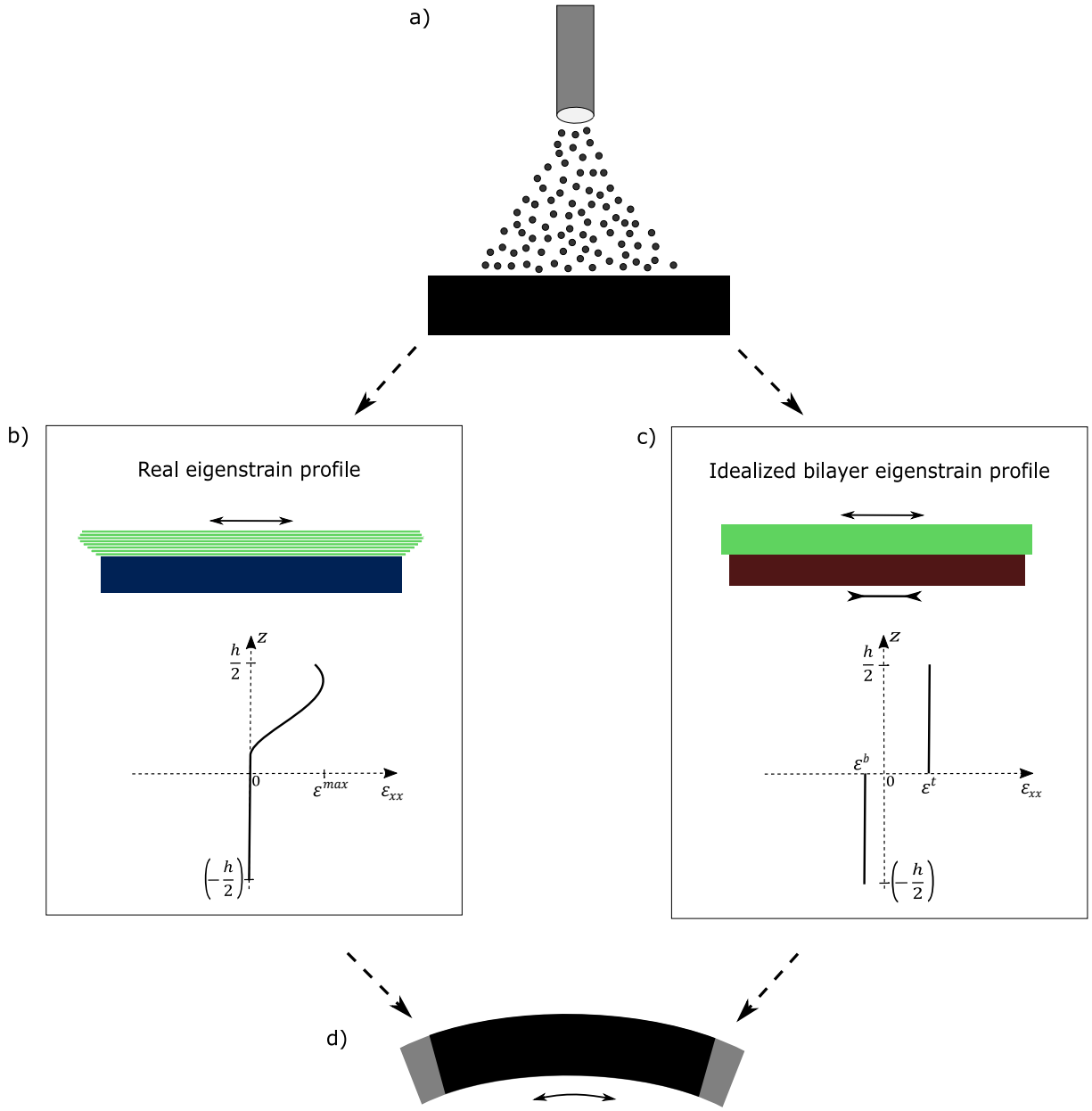

Fig. 2. The real and idealized eigenstrain profiles induced by uniform shot peening of a plate. We denote the plate thickness as h. The coordinate z goes along the thickness and measures form the midplane. a) The plate undergoes uniform shot peening (side view). b) The through-thickness eigenstrain profile is nonuniform along z, and its peak value ε^{max} is close to the surface [7]. Its effect is accurately simulated by virtually dividing the plate into thin layers and imposing different eigenstrain to each of the layers thus reproducing the profile shape. c) We idealize the eigenstrain profile and represent the plate as a bilayer consisting of two layers of the thickness $h/2$. The eigenstrain ε^t and ε^b assigned to each of the layers is derived from the real eigenstrain profile by equating the total eigenstrain and the first eigenstrain moment. d) Both real and idealized eigenstrain profiles lead to the same deformed shape, which is bent and stretched with respect to the initial state.

words, it describes the local stretching of the surface. The 2×2 matrix containing coefficients of the first fundamental form $\mathbf{a}(x, y)$ is computed as:

$$\mathbf{a}\,(x, y) = \begin{bmatrix} \partial_x \vec{m} \cdot \partial_x \vec{m} & \partial_x \vec{m} \cdot \partial_y \vec{m} \\ \partial_y \vec{m} \cdot \partial_x \vec{m} & \partial_y \vec{m} \cdot \partial_y \vec{m} \end{bmatrix}, \tag{7}$$

where $\partial_x \vec{m} = \partial \vec{m}/\partial x$ and $\partial_y \vec{m} = \partial \vec{m}/\partial y$ are two vectors tangent to the mid-surface at the point $\vec{m}(x, y)$. If a certain area of the surface does not undergo any stretching, the first fundamental form in this area is represented by the identity matrix $\mathbf{I}$.

Together with the first fundamental form, the second fundamental form determines local curvatures on a surface. The matrix containing its coefficients $\mathbf{b}(x, y)$ is computed as:

$$\mathbf{b}(x, y) = \begin{bmatrix} \partial_{xx} \vec{m} \cdot \vec{n} & \partial_{xy} \vec{m} \cdot \vec{n} \\ \partial_{yx} \vec{m} \cdot \vec{n} & \partial_{yy} \vec{m} \cdot \vec{n} \end{bmatrix} = - \begin{bmatrix} \partial_x \vec{m} \cdot \partial_x \vec{n} & \partial_x \vec{m} \cdot \partial_y \vec{n} \\ \partial_y \vec{m} \cdot \partial_x \vec{n} & \partial_y \vec{m} \cdot \partial_y \vec{n} \end{bmatrix}, \tag{8}$$

where $\partial_{xx} \vec{m}$, $\partial_{xy} \vec{m}$ and $\partial_{yy} \vec{m}$ denote the second derivatives of $\vec{m}(x, y)$. If a surface is locally flat, its second fundamental form at this area is described by the zero matrix, because all second derivatives of the mapping $\vec{m}$ are orthogonal to the normal vector $\vec{n}$.

The two fundamental forms define a unique surface up to solid body motions. The surface is integral if its fundamental forms are *compatible*, i.e., if they satisfy three partial differential equations called the Gauss–Peterson–Mainardi–Codazzi (GPMC) equations [25]. Hence, the two *final* fundamental forms of a non-Euclidean plate are compatible, while its *rest* fundamental forms are not. This phenomenon illustrated in Fig. 3 is also called *geometric incompatibility.*

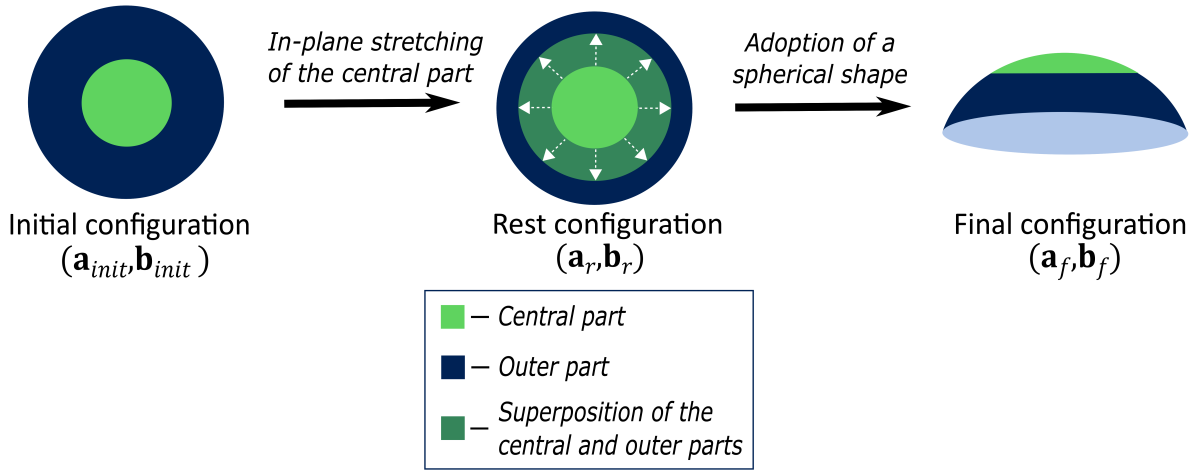

Fig. 3. An example of geometric incompatibility inspired by [14]. The initial configuration described by the fundamental forms $(\mathbf{a}_{init}, \mathbf{b}_{init})$ is a flat unstretched disc, so that $\mathbf{a}_{init}$ is the identity matrix and $\mathbf{b}_{init}$ is the zero matrix along the whole surface. The rest configuration $(\mathbf{a}_r, \mathbf{b}_r)$ prescribes isotropic in-plane stretching of the central part (green) while conserving the flat shape, so that $\mathbf{a}_r \neq \mathbf{a}_{init}$ and $\mathbf{b}_r = \mathbf{b}_{init}$. In the general case, $\mathbf{b}_r$ can be different from $\mathbf{b}_{init}$ as well. The rest fundamental forms are incompatible, because the adoption of the rest configuration means superposition of the inner (green) part and the outer (blue) part of the disc and thus loss of integrity. In order to conserve its integrity, the disc adopts a curved final configuration $(\mathbf{a}_f, \mathbf{b}_f)$ described by compatible fundamental forms. However, the disc stays residually stressed in its final configuration.

Elastic energy and the forward problem resolution

In the terms of the theory of non-Euclidean plates, the forward problem consists in determining the final configuration as a function of the rest configuration. First, we consider the simple case of an initially flat *monolayer* plate, which is subjected to a rest configuration described by the incompatible fundamental forms $\mathbf{a}_r$ and $\mathbf{b}_r$. The rest and final configurations of such a plate are related through the elastic energy functional. We denote the final fundamental forms as $\mathbf{a}_f$ and $\mathbf{b}_f$ and we express the elastic energy E_{ML} of an integral monolayer plate as [19]:

$$E_{ML} = \frac{1}{2}\int_U \left[\frac{h}{4}\left\|\mathbf{a}_r^{-1}\mathbf{a}_f - \mathbf{I}\right\|_e^2 + \frac{h^3}{12}\left\|\mathbf{a}_r^{-1}(\mathbf{b}_f - \mathbf{b}_r)\right\|_e^2\right]\sqrt{\det \mathbf{a}_r}\, dxdy. \tag{9}$$

In this expression we have introduced the elastic norm $\|\mathbf{A}\|_e^2 = \alpha Tr^2(\mathbf{A}) + 2\beta Tr(\mathbf{A}^2)$ with coefficients $\alpha = Y\nu/(1-\nu^2)$ and $\beta = Y/(2+2\nu)$. Here, Y is the Young modulus and ν is the Poisson's

ratio.

A zero elastic energy means that the final configuration perfectly coincides with the rest one. If the rest fundamental forms are incompatible, an integral plate adopts an equilibrated final configuration that minimizes the elastic energy under constraints that $\mathbf{a}_f$ and $\mathbf{b}_f$ be compatible. The first term of the elastic energy functional represents the stretching energy, and the second term defines the bending energy. If the plate is thin, the bending term is small in comparison to the stretching one, so the plate stretches as prescribed by the rest configuration but adopts a different curvature. In other words, $\mathbf{a}_f$ in this case is close to $\mathbf{a}_r$, but $\mathbf{b}_f$ can be largely different from $\mathbf{b}_r$. On the contrary, a thick plate adopts the curvature prescribed by the rest configuration but stretches in a different way, so that $\mathbf{b}_f$ is close to $\mathbf{b}_r$ [12].

Now let us consider a *bilayer* plate, where each layer is of thickness $h/2$. We suppose that the plate is initially flat, and that its layers exhibit nonuniform in-plane swelling or shrinking. The eigenstrain introduced in each layer may vary along the surface, but it is constant along the layer thickness. Locally, the eigenstrain is different for each layer, so that the rest first fundamental forms of each layer ($\mathbf{a}_{r,t}$ and $\mathbf{a}_{r,b}$) are different. Matrices $\mathbf{a}_{r,t}$ and $\mathbf{a}_{r,b}$ contain information on the principal eigenstrain direction and magnitude on the top and bottom layers respectively. Essentially, the $\mathbf{a}_{r,t}$ and $\mathbf{a}_{r,b}$ describe stretching that the layers would adopt if they were not attached together. By assuming that each layer expands uniformly across its thickness, all terms of the rest second fundamental form of each layer are zero along the whole surface:

$$\mathbf{b}_{r,t} = \mathbf{b}_{r,b} = \begin{bmatrix} 0 & 0 \\ 0 & 0 \end{bmatrix}. \tag{10}$$

Accordingly, $\mathbf{a}_{r,t}$ and $\mathbf{a}_{r,b}$ fully describe the rest configuration. The forward problem consists in finding $\mathbf{a}_f$ and $\mathbf{b}_f$ that describe the shape of the integral plate mid-surface after reconfiguration. The reconfiguration process for the bilayer case is presented in Fig. 4. Following [19], we express the elastic energy of the bilayer plate as the sum of the elastic energies of two monolayers of

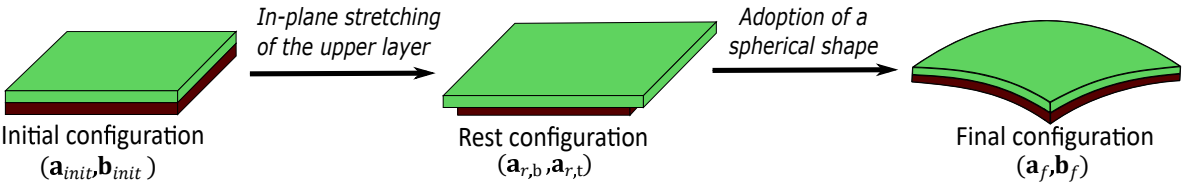

Fig. 4. An example of geometric incompatibility in a bilayer plate inspired by [19]. The initial configuration described by the fundamental forms $(\mathbf{a}_{init}, \mathbf{b}_{init})$ is a flat unstretched rectangular plate, so that $\mathbf{a}_{init}$ is the identity matrix and $\mathbf{b}_{init}$ is the zero matrix along the whole surface. The rest configuration $(\mathbf{a}_{r,t}, \mathbf{a}_{r,b})$ prescribes isotropic in-plane stretching of the top layer and shrinking of the bottom layer while conserving the flat shape, so that $\mathbf{a}_{r,t} \neq \mathbf{a}_{init}$, $\mathbf{a}_{r,b} \neq \mathbf{a}_{init}$, $\mathbf{b}_{r,t} = \mathbf{b}_{init}$ and $\mathbf{b}_{r,b} = \mathbf{b}_{init}$. Since peen forming causes in-plane eigenstrain we do not consider cases when $\mathbf{b}_{r,t} \neq \mathbf{0}$ and $\mathbf{b}_{r,b} \neq \mathbf{0}$ for our simulations, so that the rest configuration is entirely described by $(\mathbf{a}_{r,t}, \mathbf{a}_{r,b})$. Adoption of the rest configuration means dissection of the plate in two layers. Instead, the plate adopts an integral but residually stressed final configuration $(\mathbf{a}_f, \mathbf{b}_f)$ described by compatible fundamental forms.

thickness $h/2$. After integration over the total plate thickness we obtain:

$$\begin{aligned} E_{BL} = \frac{1}{2}\int_U \left[\frac{h}{8}\left\|\mathbf{a}_{r,b}^{-1}\mathbf{a}_f - \mathbf{I}\right\|_e^2 + \frac{h^3}{24}\left\|\mathbf{a}_{r,b}^{-1}\mathbf{b}_f\right\|_e^2 + \frac{h^2}{8}\left\langle\left(\mathbf{a}_{r,b}^{-1}\mathbf{a}_f - \mathbf{I}\right), \mathbf{a}_{r,b}^{-1}\mathbf{b}_f\right\rangle_e\right]\sqrt{\det \mathbf{a}_{r,b}}\, dxdy \\ + \frac{1}{2}\int_U \left[\frac{h}{8}\left\|\mathbf{a}_{r,t}^{-1}\mathbf{a}_f - \mathbf{I}\right\|_e^2 + \frac{h^3}{24}\left\|\mathbf{a}_{r,t}^{-1}\mathbf{b}_f\right\|_e^2 - \frac{h^2}{8}\left\langle\left(\mathbf{a}_{r,t}^{-1}\mathbf{a}_f - \mathbf{I}\right), \mathbf{a}_{r,t}^{-1}\mathbf{b}_f\right\rangle_e\right]\sqrt{\det \mathbf{a}_{r,t}}\, dxdy. \end{aligned} \tag{11}$$

The elastic energy inner product $\langle\cdot,\cdot\rangle_e$ introduced in this context defines the following operation: $\langle \mathbf{A}, \mathbf{B}\rangle_e = \alpha Tr\left(\mathbf{A}\right) Tr\left(\mathbf{B}\right) + 2\beta Tr(\mathbf{AB})$. Similarly to the monolayer case, the plate adopts a curved final configuration $(\mathbf{a}_f, \mathbf{b}_f)$ that minimizes the elastic energy. Generally, the final configuration is not unique, and moreover, the plate can get stuck in a configuration corresponding to a local energetic minimum on its way to the global minimum.

For a bilayer subjected to any rest configuration $(\mathbf{a}_{r,b}, \mathbf{a}_{r,t})$, there exists an equivalent monolayer that morphs into the same final configuration $(\mathbf{a}_f, \mathbf{b}_f)$ after being subjected to a rest configuration $(\mathbf{a}_r, \mathbf{b}_r)$. The relation between $(\mathbf{a}_{r,b}, \mathbf{a}_{r,t})$ and $(\mathbf{a}_r, \mathbf{b}_r)$ is derived by equating the monolayer energy (Eqn. 9) and the bilayer energy (Eqn. 11) and is expressed as [19]:

$$\begin{cases} \mathbf{a}_r = \dfrac{1}{2}\left(\mathbf{a}_{r,b} + \mathbf{a}_{r,t}\right); \\ \mathbf{b}_r = \dfrac{3}{4h}\left(\mathbf{a}_{r,b} - \mathbf{a}_{r,t}\right). \end{cases} \tag{12}$$

Inversely,

$$\begin{cases} \mathbf{a}_{r,t} = \mathbf{a}_r - \dfrac{2h}{3}\mathbf{b}_r; \\ \mathbf{a}_{r,b} = \mathbf{a}_r + \dfrac{2h}{3}\mathbf{b}_r. \end{cases} \tag{13}$$

Here, the monolayer and bilayer plates are supposed to have the same initial geometry and the same total thickness h.

The inverse problem resolution

The inverse problem consists in determining the rest configuration that leads to a target configuration due to the elastic material response. In the bilayer case, it means finding the rest first fundamental forms of the bottom and top layers $\mathbf{a}_{r,b}$ and $\mathbf{a}_{r,t}$, respectively as a function of the target shape described by $\mathbf{a}_{tar}$ and $\mathbf{b}_{tar}$. As each fundamental form is represented by a symmetric 2×2 matrix, the target configuration is locally defined by six scalar variables. At the same time, the rest configuration also has six degrees of freedom, so the problem admits an analytical solution provided by Eqn. (13). Moreover, the final configuration obtained with this solution is stress-free [19]. A practical application of the analytically calculated solution means inducing local *orthotropic* eigenstrain, so that $\varepsilon_{11}(x, y, z) \neq \varepsilon_{22}(x, y, z)$, where ε_{11} and ε_{22} are the local principal eigenstrains. In other words, one has to locally control the principal strain directions and the strain magnitude along both directions, and this – at each of the two layers separately. Such local control over the direction of expansions is generally not possible with shot peen forming, because here we assume that shot peening induces local *isotropic* in-plane strain. Thus, at each point we only

control two degrees of freedom: $\varepsilon^t(x, y)$ and $\varepsilon^b(x, y)$. Hence, we have control over fewer degrees of freedom than input variables. In this case, a solution leading exactly to the target shape may not exist, so we can only numerically optimize $\mathbf{a}_{r,t}$ and $\mathbf{a}_{r,b}$. The uniqueness of solution is not guaranteed either.

METHODOLOGY

Our method for the inverse problem resolution consists in the iterative correction of the peening pattern on a local scale until convergence is reached within a tolerance and subsequent grouping of the pattern. The grouping algorithm divides the pattern in zones treated with predefined peening regimes.

Iterative adjustment of the peening pattern

The iterative method idea is to adjust the rest configuration by comparing the local stretching and curvature of the current shape with the stretching and curvature of the target shape. The current shape is computed at each iteration through a numerical resolution of the forward problem. For the initial guess, we use analytical expressions to approximately define an appropriate rest configuration.

The initial guess

We characterize the target configuration in terms of fundamental forms $(\mathbf{a}_{tar}, \mathbf{b}_{tar})$. Let us consider the monolayer rest configuration $\left(\mathbf{a}_r^{ortho}, \mathbf{b}_r^{ortho}\right)$ described by $\mathbf{a}_r^{ortho} = \mathbf{a}_{tar}$ and $\mathbf{b}_r^{ortho} = \mathbf{b}_{tar}$, that in a general case prescribes local orthotropic in-plane strain. According to the expression for the elastic energy (Eqn. 9), imposition of this rest configuration makes the plate adopt exactly the target configuration, because the elastic energy in this case equals zero. Following [19], we express the equivalent bilayer rest configuration $\left(\mathbf{a}_{r,t}^{ortho}, \mathbf{a}_{r,b}^{ortho}\right)$ using Eqn. (13):

$$\begin{cases} \mathbf{a}_{r,t}^{ortho} = \mathbf{a}_{r}^{ortho} - \dfrac{2h}{3}\mathbf{b}_{r}^{ortho}; \\ \mathbf{a}_{r,b}^{ortho} = \mathbf{a}_{r}^{ortho} + \dfrac{2h}{3}\mathbf{b}_{r}^{ortho}. \end{cases} \tag{14}$$

Equivalently, using the definition of $\left(\mathbf{a}_{r}^{ortho}, \mathbf{b}_{r}^{ortho}\right)$ we rewrite:

$$\begin{cases} \mathbf{a}_{r,t}^{ortho} = \mathbf{a}_{tar} - \dfrac{2h}{3}\mathbf{b}_{tar}; \\ \mathbf{a}_{r,b}^{ortho} = \mathbf{a}_{tar} + \dfrac{2h}{3}\mathbf{b}_{tar}. \end{cases} \tag{15}$$

Thus, application of the rest configuration $\left(\mathbf{a}_{r,t}^{ortho}, \mathbf{a}_{r,b}^{ortho}\right)$ leads to the target shape $(\mathbf{a}_{tar}, \mathbf{b}_{tar})$. However, this configuration implies local orthotropic eigenstrain, which is not feasible with shot peen forming. We comply with this constraint and find a suitable local isotropic eigenstrain based on this prediction. To that end, we first compute the local eigenstrains in the principal directions in the top $(\varepsilon_{11}^{t},\, \varepsilon_{22}^{t})$ and bottom $(\varepsilon_{11}^{b},\, \varepsilon_{22}^{b})$ layers of the bilayer prescribed by $\mathbf{a}_{r,t}^{ortho}$ and $\mathbf{a}_{r,b}^{ortho}$, respectively. Next, we take their averages ε_{avg}^{t} and ε_{avg}^{b} and impose them locally in all in-plane directions thus making the initial guess.

To find $(\varepsilon_{11}^{t},\, \varepsilon_{22}^{t})$ and $(\varepsilon_{11}^{b},\, \varepsilon_{22}^{b})$ we perform a spectral decomposition of $\mathbf{a}_{r,t}^{ortho}$ and $\mathbf{a}_{r,b}^{ortho}$, respectively [19]. At the top layer, the distortions prescribed by $\mathbf{a}_{r,t}^{ortho}$ imply stretching by a factor of $(\varepsilon_{11}^{t}+1)$ in the first principal direction and by a factor of $(\varepsilon_{22}^{t}+1)$ in the orthogonal second principal direction. The first principal direction is rotated by an angle of θ^{t} with respect to the x-axis. At the bottom layer, the stretch factors are $(\varepsilon_{11}^{b}+1)$ and $(\varepsilon_{22}^{b}+1)$, and the first principal direction is rotated by an angle of θ^{b} with respect to the x-axis. The initial configuration is unstretched, so its first fundamental form $\mathbf{a}_{init}$ is represented by the identity matrix:

$$\mathbf{a}_{init} = \mathbf{I}. \tag{16}$$

Consequently, the eigenvalues of $\mathbf{a}_t^{ortho}$ equal $(\varepsilon_{11}^t + 1)^2$ and $(\varepsilon_{22}^t + 1)^2$, and the eigenvalues of $\mathbf{a}_b^{ortho}$ equal $(\varepsilon_{11}^b + 1)^2$ and $(\varepsilon_{22}^b + 1)^2$, so that:

$$\mathbf{a}_{r,j}^{ortho} = \begin{bmatrix} \cos(\theta^j) & -sin(\theta^j) \\ \sin(\theta^j) & \cos(\theta^j) \end{bmatrix}^T \begin{bmatrix} (\varepsilon_{11}^j + 1)^2 & 0 \\ 0 & (\varepsilon_{22}^j + 1)^2 \end{bmatrix} \begin{bmatrix} \cos(\theta^j) & -sin(\theta^j) \\ \sin(\theta^j) & \cos(\theta^j) \end{bmatrix}, \quad \text{for} \quad j = t, b. \tag{17}$$

We deduce the local eigenstrain in the principal directions $(\varepsilon_{11}^t, \varepsilon_{22}^t)$ and $(\varepsilon_{11}^b, \varepsilon_{22}^b)$ from the eigenvalues and calculate the average local eigenstrain ε_{avg}^t and ε_{avg}^b for both layers:

$$\varepsilon_{avg}^j = \frac{\varepsilon_{11}^j + \varepsilon_{22}^j}{2}, \quad \text{for} \quad j = t, b. \tag{18}$$

We impose the local isotropic eigenstrain ε_{avg}^t and ε_{avg}^b on the top and bottom layers, respectively, thus making the initial guess. The bilayer rest fundamental forms $\mathbf{a}_{r,t}$ and $\mathbf{a}_{r,b}$ corresponding to this strain are expressed as:

$$\mathbf{a}_{r,j} = \begin{bmatrix} (\varepsilon_{avg}^j + 1)^2 & 0 \\ 0 & (\varepsilon_{avg}^j + 1)^2 \end{bmatrix}, \quad \text{for} \quad j = t, b. \tag{19}$$

We substitute $(\mathbf{a}_{r,t}, \mathbf{a}_{r,b})$ to the bilayer elastic energy functional (Eqn. 11) and find the *current* shape

$(\mathbf{a}_c, \mathbf{b}_c)$ that minimizes the elastic energy.

Following Eqn. (12), it is possible to find equivalent monolayer rest fundamental forms $(\mathbf{a}_r, \mathbf{b}_r)$. Prescription of the rest fundamental forms $(\mathbf{a}_r, \mathbf{b}_r)$ to a monolayer plate leads to the same current shape $(\mathbf{a}_c, \mathbf{b}_c)$ as the prescription of $(\mathbf{a}_{r,t}, \mathbf{a}_{r,b})$ to a bilayer plate. Essentially, $(\mathbf{a}_r, \mathbf{b}_r)$ can be viewed as the rest configuration imposed on the bilayer mid-surface. The forms $\mathbf{a}_r$ and $\mathbf{b}_r$ may be incompatible as they were defined analytically, but $\mathbf{a}_c$ and $\mathbf{b}_c$ are always compatible because they describe a surface in Euclidean space. Consequently, $(\mathbf{a}_c, \mathbf{b}_c)$ are typically different from $(\mathbf{a}_r, \mathbf{b}_r)$.

Adjustment of the local stretching

In the previous subsection, we defined a procedure to obtain a quick estimate of the inverse problem by solving for orthotropic expansions and averaging them to estimate isotropic expansions. In this subsection and the next, we seek to iteratively correct these expansions by using only local information.

As the rest configuration $(\mathbf{a}_{r,t}, \mathbf{a}_{r,b})$ prescribes local *isotropic* in-plane strain, we measure stretching in terms of local areas. The area A of each region of the surface constrained by $(x, y) \in U_1 \subset \mathbb{R}^2$ is expressed in terms of the first fundamental form $\mathbf{a}$ as $A = \iint_{U_1} \sqrt{det(\mathbf{a})}\, dxdy$. The first fundamental form is considered constant inside small regions, so we conclude that the current area of each small region A_c and its target area A_{tar} are related as:

$$\frac{A_{tar}}{A_c} \approx \frac{\sqrt{\det(\mathbf{a}_{tar})}}{\sqrt{\det(\mathbf{a}_c)}} = k_A. \tag{20}$$

This means that if we locally multiply $\mathbf{a}_c$ by the coefficient k_A, then the current area will equal that of the target. However, we are only able to influence $\mathbf{a}_c$ indirectly through the adjustment of $\mathbf{a}_r$. Consequently, as a part of the iterative procedure, we multiply $\mathbf{a}_r$ by k_A and thus obtain the equivalent monolayer rest fundamental form $\mathbf{a}_r^{new}$ to be imposed during the subsequent iteration:

$$\mathbf{a}_r^{new} = k_A \mathbf{a}_r. \tag{21}$$

The $\mathbf{a}_r^{new}$ may be different from the current first fundamental form on the subsequent iteration $\mathbf{a}_c^{new}$, and thus this correction of the rest fundamental form does not lead to an exact solution but allows to approach it. In other words, multiplication of $\mathbf{a}_r$ by k_A does not correct the local area exactly by the coefficient k_A but reduces the difference between the current local stretching and the target one.

Adjustment of the local curvature

We characterize the surface curvature in terms of the local mean curvature H. By definition, H is the average of two local principal curvatures κ_1 and κ_2, that are computed as eigenvalues of the shape operator $\mathbf{S} = \mathbf{a}^{-1}\mathbf{b}$ [26]. We compute the local ratios k_H between the current mean curvatures H_c and the target mean curvatures H_{tar} and assign an upper threshold δ for $|k_H|$:

$$\begin{cases} k_H = \dfrac{H_{tar}}{H_c} \quad \text{for} \quad \left|\dfrac{H_{tar}}{H_c}\right| < \delta; \\ k_H = \delta \cdot sgn\left(\dfrac{H_{tar}}{H_c}\right) \quad \text{for} \quad \left|\dfrac{H_{tar}}{H_c}\right| \geq \delta. \end{cases} \tag{22}$$

Here, H_{tar} is the average of the two eigenvalues of $\mathbf{S}_{tar} = \mathbf{a}_{tar}^{-1}\mathbf{b}_{tar}$, and H_c is the average of the two eigenvalues of $\mathbf{S}_c = \mathbf{a}_c^{-1}\mathbf{b}_c$. The threshold δ is assigned in order to deal with special cases when $|H_c|$ is small. Provided that multiplication of a matrix by a constant multiplies its eigenvalues by the same constant, the multiplication of $\mathbf{S}_c$ by k_H would make the current local mean curvatures equal to those of the target. As we are unable to adjust any of the current fundamental forms $(\mathbf{a}_c, \mathbf{b}_c)$ directly, we influence them through adjustment of the rest fundamental forms $(\mathbf{a}_r, \mathbf{b}_r)$ in order to get:

$$\mathbf{S}_r^{new} = k_H \mathbf{S}_r = k_H \mathbf{a}_r^{-1} \mathbf{b}_r = k_H k_A \frac{\mathbf{a}_r^{-1}}{k_A} \mathbf{b}_r = k_H k_A \left(\mathbf{a}_r^{new}\right)^{-1} \mathbf{b}_r. \tag{23}$$

Thus, we define:

$$\mathbf{b}_r^{new} = k_H k_A \mathbf{b}_r. \tag{24}$$

Once the $\mathbf{a}_r^{new}$ and $\mathbf{b}_r^{new}$ are found, we compute the bilayer rest fundamental forms $(\mathbf{a}_{r,t}^{new}, \mathbf{a}_{r,b}^{new})$ as:

$$\begin{cases} \mathbf{a}_{r,t}^{new} = \mathbf{a}_r^{new} - \dfrac{2h}{3} \mathbf{b}_r^{new}; \\ \mathbf{a}_{r,b}^{new} = \mathbf{a}_r^{new} + \dfrac{2h}{3} \mathbf{b}_r^{new}. \end{cases} \tag{25}$$

Next, we substitute $(\mathbf{a}_{r,t}^{new}, \mathbf{a}_{r,b}^{new})$ to the bilayer elastic energy functional (Eqn. 11) and find the current shape $(\mathbf{a}_c^{new}, \mathbf{b}_c^{new})$ that minimizes the elastic energy.

Subsequent iterations and stop criterion

We compare the current shape with the target shape and recalculate the bilayer rest fundamental forms until a convergence criterion is satisfied. The convergence criterion is based on the calculation of the Hausdorff distance d_H between the new current configuration $\mathcal{C}_c^{new}$ defined by $(\mathbf{a}_c^{new}, \mathbf{b}_c^{new})$ and the current configuration from the previous iteration $\mathcal{C}_c$ defined by $(\mathbf{a}_c, \mathbf{b}_c)$. We nondimensionalize d_H by the square root of the total area of the plate in its initial configuration A_{total}. We stop iterating either when a predefined maximal number of iterations M is reached, or

when the nondimensionalized Hausdorff distance becomes inferior to a chosen threshold τ:

$$\frac{d_H(C_c, C_c^{new})}{\sqrt{A_{total}}} < \tau. \tag{26}$$

Calculation of the adjusted eigenstrain

We denote the bilayer *final rest* fundamental forms, i.e., the ones obtained on the last iteration, as $(\mathbf{a}_{rf,t}\ , \mathbf{a}_{rf,b})$. To relate them with peen forming parameters, we determine the recalculated eigenstrain $(\varepsilon^{rf,t}, \varepsilon^{rf,b})$.

Provided that the iterative adjustment implies only addition, subtraction and multiplication by a constant of diagonal matrices, the $\mathbf{a}_{rf,t}$ and $\mathbf{a}_{rf,b}$ are diagonal. Moreover, the imposed local eigenstrain $(\varepsilon^{rf,t}, \varepsilon^{rf,b})$ is isotropic, so $\mathbf{a}_{rf,t}$ and $\mathbf{a}_{rf,b}$ have the following form:

$$\mathbf{a}_{rf,j} = \begin{bmatrix} \left(\varepsilon^{rf,j}+1\right)^2 & 0 \\ 0 & \left(\varepsilon^{rf,j}+1\right)^2 \end{bmatrix}, \quad \text{for} \quad j = t, b. \tag{27}$$

Consequently,

$$\varepsilon^{rf,j} = \sqrt{a^{11}_{rf,j}} - 1, \quad \text{for} \quad j = t, b. \tag{28}$$

Numerical implementation

We mesh the plate mid-surface with triangular elements and follow the energy calculation strategy presented in [17] [27]. The first and the second fundamental forms are estimated separately for each element and are constant inside the element. The global elastic energy is calculated as

a sum of local energetical contributions from all the elements.

The first fundamental form on a triangular element such as that schematized in Fig. 5 depends entirely on the coordinates of the vertices. The three vertices are defined by position vectors $\vec{v}_0$, $\vec{v}_1$ and $\vec{v}_2$, and the edge vectors constituting the triangle are expressed as: $\vec{e}_0 = \vec{v}_1 - \vec{v}_0$, $\vec{e}_1 = \vec{v}_2 - \vec{v}_1$, $\vec{e}_2 = \vec{v}_0 - \vec{v}_2$. These vectors are tangent to the plane containing the triangle, so following Eqn. (7), the first fundamental form on a triangular element is computed as:

$$\mathbf{a} = \begin{bmatrix} \vec{e}_1 \cdot \vec{e}_1 & \vec{e}_1 \cdot \vec{e}_2 \\ \vec{e}_2 \cdot \vec{e}_1 & \vec{e}_2 \cdot \vec{e}_2 \end{bmatrix}. \tag{29}$$

In a general case of isotropic eigenstrain ε^r imposed on a triangular element, its rest first fundamental form $\mathbf{a}_r$ is expressed as:

$$\mathbf{a}_r = \begin{bmatrix} \vec{e}_1^{\,init} \cdot \vec{e}_1^{\,init} & \vec{e}_1^{\,init} \cdot \vec{e}_2^{\,init} \\ \vec{e}_2^{\,init} \cdot \vec{e}_1^{\,init} & \vec{e}_2^{\,init} \cdot \vec{e}_2^{\,init} \end{bmatrix} \begin{bmatrix} (\varepsilon^r + 1)^2 & 0 \\ 0 & (\varepsilon^r + 1)^2 \end{bmatrix} = \mathbf{a}_{init} \begin{bmatrix} (\varepsilon^r + 1)^2 & 0 \\ 0 & (\varepsilon^r + 1)^2 \end{bmatrix}, \tag{30}$$

where $\vec{e}_1^{\,init}$, $\vec{e}_2^{\,init}$, $\vec{e}_3^{\,init}$ are the edge vectors in the initial configuration and $\mathbf{a}_{init}$ is the element first fundamental form in its initial configuration. Otherwise, if an orthotropic in-plane strain is imposed, then the rest first fundamental form $\mathbf{a}_r^{ortho}$ becomes:

$$\mathbf{a}_r^{ortho} = \mathbf{a}_{init} \begin{bmatrix} \cos(\theta) & -sin(\theta) \\ \sin(\theta) & \cos(\theta) \end{bmatrix}^T \begin{bmatrix} (\varepsilon_{11}^r + 1)^2 & 0 \\ 0 & (\varepsilon_{22}^r + 1)^2 \end{bmatrix} \begin{bmatrix} \cos(\theta) & -sin(\theta) \\ \sin(\theta) & \cos(\theta) \end{bmatrix}, \tag{31}$$

where ε_{11}^r and ε_{22}^r define the eigenstrain imposed in the principal directions and θ stands for the

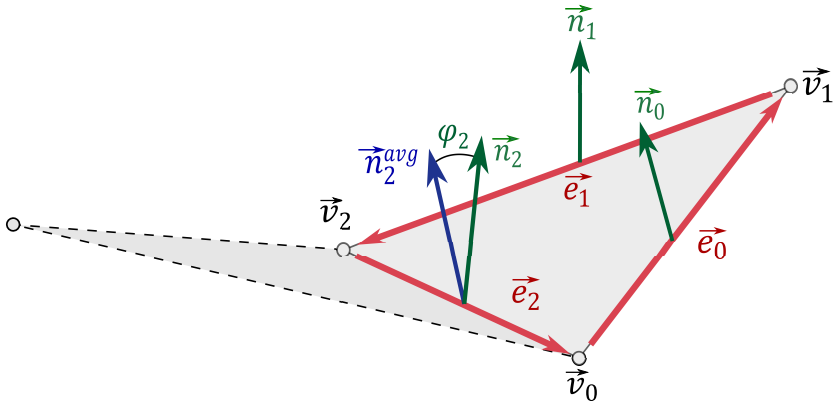

Fig. 5. A triangular mesh element and vectors that determine local fundamental forms: the vertex position vectors ($\vec{v}_0$, $\vec{v}_1$ and $\vec{v}_2$), the edge vectors ($\vec{e}_0$, $\vec{e}_1$ and $\vec{e}_2$) and the mid-edge normals ($\vec{n}_0$, $\vec{n}_1$ and $\vec{n}_2$). The mid-edge normals are perpendicular to the edge, and their direction is determined by the angle of inclination with respect to the average normal of the two adjacent faces. Thus, the direction of $\vec{n}_2$ is determined by the angle φ_2. This angle is measured with respect to $\vec{n}_{avg}$, which is the average normal of the two faces that share the edge $\vec{e}_2$.

angle between the first principal direction and the x axis.

The second fundamental form defines the surface curvature, so the information about surface normals is required. In this connection we introduce a unit normal vector $\vec{n}_i,\ i = 1, 2, 3$ at the center of each edge of the mesh (the *edge-director*). This vector is normal to the edge, and its angle of inclination $\varphi_i,\ i = 1, 2, 3$ in the plane perpendicular to the edge provides a supplementary degree of freedom. This angle is measured with respect to the average of the adjacent face normals [27]. A finite-difference approximation of the derivatives appearing in Eqn. (8) yields the following expression for the second fundamental form of a triangular element:

$$\mathbf{b} = \begin{bmatrix} \vec{e}_1 \cdot 2(\vec{n}_0 - \vec{n}_2) & \vec{e}_1 \cdot 2(\vec{n}_1 - \vec{n}_0) \\ \vec{e}_1 \cdot 2(\vec{n}_1 - \vec{n}_0) & \vec{e}_2 \cdot 2(\vec{n}_1 - \vec{n}_0) \end{bmatrix} = \begin{bmatrix} \vec{e}_1 \cdot 2(\vec{n}_0 - \vec{n}_2) & -\vec{e}_1 \cdot \vec{n}_0 \\ -\vec{e}_1 \cdot \vec{n}_0 & \vec{e}_2 \cdot 2(\vec{n}_1 - \vec{n}_0) \end{bmatrix}. \tag{32}$$

According to Eqn. (11), the global elastic energy for a plate composed of K triangular elements is expressed in terms of local fundamental forms as:

$$
\begin{aligned}
E_{BL} = \frac{1}{2}\sum_{k=1}^{K}\Bigg[\frac{h_k}{8}\left\|(\mathbf{a}_{r,b}^{-1})_k(\mathbf{a}_f)_k - \mathbf{I}\right\|_e^2 + \frac{(h_k)^3}{24}\left\|(\mathbf{a}_{r,b}^{-1})_k(\mathbf{b}_f)_k\right\|_e^2 \\
+\frac{(h_k)^2}{8}\left\langle\left((\mathbf{a}_{r,b}^{-1})_k(\mathbf{a}_f)_k - \mathbf{I}\right),(\mathbf{a}_{r,b}^{-1})_k(\mathbf{b}_f)_k\right\rangle_e\Bigg]\sqrt{\det(\mathbf{a}_{r,b})_k} \\
+\frac{1}{2}\sum_{k=1}^{K}\Bigg[\frac{h_k}{8}\left\|(\mathbf{a}_{r,t}^{-1})_k(\mathbf{a}_f)_k - \mathbf{I}\right\|_e^2 + \frac{(h_k)^3}{24}\left\|(\mathbf{a}_{r,t}^{-1})_k(\mathbf{b}_f)_k\right\|_e^2 \\
-\frac{(h_k)^2}{8}\left\langle\left((\mathbf{a}_{r,t}^{-1})_k(\mathbf{a}_f)_k - \mathbf{I}\right),(\mathbf{a}_{r,t}^{-1})_k(\mathbf{b}_f)_k\right\rangle_e\Bigg]\sqrt{\det(\mathbf{a}_{r,t})_k}.
\end{aligned}
\tag{33}
$$

The local plate thickness h_k can be different for each element. Similarly, the local Young's modulus Y_k and the Poisson's ratio ν_k can vary along the plate.

As follows from Eqn. (30), the element's rest first fundamental forms $\mathbf{a}_{r,t}$ and $\mathbf{a}_{r,b}$ for the isotropic growth case are defined by the imposed local eigenstrain ε^t and ε^b and the initial vertex positions $\vec{v}_i^{\,init},\ i = 1,2,3$. At the same time, according to Eqn. (29) and Eqn. (32), the two final fundamental forms $\mathbf{a}_f$ and $\mathbf{b}_f$ are defined by the final vertex positions $\vec{v}_i^{\,f},\ i = 1,2,3$, and final angles of inclination of the edge directors $\varphi_i^f,\ i = 1,2,3$. Numerically, the forward problem consists in minimizing the global elastic energy functional (Eqn. 33) with respect to $\vec{v}_i^{\,f}$ and φ_i^f provided with $\vec{v}_i^{\,init}$, ε^t and ε^b. We perform the minimization using a quasi-Newton L-BFGS algorithm [28]. The gradients of the elastic energy functional required by the minimization algorithm are computed analytically following [29]. The corresponding programming code for the forward problem resolution was developed by van Rees et al. and is publicly accessible [30].

In this implementation, the inverse problem resolution consists in finding the local eigenstrain $\varepsilon^{rf,t}$ and $\varepsilon^{rf,b}$ to be imposed on each triangular element. This means that the iterative correction of the rest fundamental forms $\mathbf{a}_{r,t}$ and $\mathbf{a}_{r,b}$ is executed on a local scale for each element separately, whilst the forward problem is resolved on each iteration on a global scale, thus reflecting the mechanics of the plate.

Algorithm 1 The inverse problem resolution

The iterative loop

while condition (26) is not satisfied and the number of iterations is below maximum **do**
  for each triangular element **do**
    Find principal curvatures (κ_1^c, κ_2^c) as eigenvalues of the shape operator $\mathbf{S}_c = \mathbf{a}_c^{-1}\mathbf{b}_c$
    Compute the current mean curvature as $H_c = 0.5\,(\kappa_1^c + \kappa_2^c)$
    Compute the current area as $A_c = \sqrt{\det(\mathbf{a}_c)}$
    Compute the ratios k_A and k_H following Eqn. (20) and Eqn. (22) respectively
    Compute the monolayer rest fundamental forms $\mathbf{a}_r$ and $\mathbf{b}_r$ following Eqn. (12) using only local information
    Compute the adjusted monolayer rest fundamental forms $\mathbf{a}_r^{new}$ and $\mathbf{b}_r^{new}$ following Eqn. (21) and Eqn. (24) respectively
    Compute the adjusted bilayer rest fundamental forms $\mathbf{a}_{r,t}^{new}$ and $\mathbf{a}_{r,b}^{new}$ following Eqn. (25)
  end for
  Substitute $\mathbf{a}_{r,t}^{new}$ and $\mathbf{a}_{r,b}^{new}$ to the bilayer elastic energy functional (Eqn. 33) and minimize it to solve the forward problem and find the current configuration $(\mathbf{a}_c^{new}, \mathbf{b}_c^{new})$
end while

The initial guess

for each triangular element **do**
  Compute the first fundamental form of the initial shape $\mathbf{a}_{init}$ following Eqn. (29)
  Compute the monolayer fundamental forms of the target shape $\mathbf{a}_{tar}$ and $\mathbf{b}_{tar}$ following Eqn. (29) and Eqn. (32) respectively
  Find principal curvatures κ_1^{tar} and κ_2^{tar} as eigenvalues of the target shape operator $\mathbf{S}_{tar} = \mathbf{a}_{tar}^{-1}\mathbf{b}_{tar}$
  Compute the target mean curvature as $H_{tar} = 0.5(\kappa_1^{tar} + \kappa_2^{tar})$
  Compute the target area as $A_{tar} = \sqrt{\det(\mathbf{a}_{tar})}$
  Compute the orthotropic bilayer rest fundamental forms $\mathbf{a}_{r,t}^{ortho}$ and $\mathbf{a}_{r,b}^{ortho}$ following Eqn. (15)
  Find eigenvalues λ_1^j and λ_2^j of $(\mathbf{a}_{init}^{-1}\mathbf{a}_{r,j}^{ortho})$ for $j = t, b$
  Compute the orthotropic eigenstrain as $\varepsilon_{ii}^j = \sqrt{\lambda_i^j} - 1$ for $i = 1, 2$ and $j = t, b$
  Compute the average eigenstrain ε_{avg}^t and ε_{avg}^b following Eqn. (18)
  Compute bilayer rest fundamental forms $\mathbf{a}_{r,t}$ and $\mathbf{a}_{r,b}$ by substituting ε_{avg}^t and ε_{avg}^b respectively for ε^r in Eqn. (30)
end for
Substitute $\mathbf{a}_{r,t}$ and $\mathbf{a}_{r,b}$ to the bilayer elastic energy functional (Eqn. 33) and minimize it to solve the forward problem and find the current configuration $(\mathbf{a}_c, \mathbf{b}_c)$

Algorithm 1 The inverse problem resolution

Final step after exiting the iterative loop

1: **for** each triangular element **do**
2: Compute the eigenstrain $\varepsilon^{rf,t}$ and $\varepsilon^{rf,b}$ prescribed by $\mathbf{a}_{rf,t} = \mathbf{a}_{r,t}^{new}$ and by $\mathbf{a}_{rf,b} = \mathbf{a}_{r,b}^{new}$ respectively following Eqn. (28)
3: **end for**

Grouping of the peening pattern

In the general case, the eigenstrains $(\varepsilon^{rf,t}, \varepsilon^{rf,b})$ provided by Alg. 1 are different for each element and can take any real values. Peen forming often deals with smoothly curved target shapes, so $(\varepsilon^{rf,t}, \varepsilon^{rf,b})$ may also vary smoothly along the surface given that these two values depend on the target shape curvature. We call the eigenstrain pattern provided by the Alg. 1 the *free* pattern. From a practical point of view, each pair $(\varepsilon^{rf,t}, \varepsilon^{rf,b})$ represents a peening regime. However, a limited number of regimes is available when peening a real part. Thus, we divide the pattern into zones with uniform prescribed eigenstrain and obtain a *grouped* pattern.

We associate all triangular elements with points on a plane with cartesian coordinates $\left(\varepsilon^t, \varepsilon^b\right)$, and the coordinates of each point k are determined by the eigenstrain $\left(\varepsilon_k^{rf,t}, \varepsilon_k^{rf,b}\right)$ assigned to the corresponding element k, as illustrated in Fig. 6. We divide the points in groups, and the group centroids are determined by the predefined peening regimes. We denote the centroid of a group n by $\left(\varepsilon_n^{cen,t}, \varepsilon_n^{cen,b}\right)$. Each point $\left(\varepsilon_k^{rf,t}, \varepsilon_k^{rf,b}\right)$ is attributed to the group with the closest centroid in terms of Euclidean distance. When all points are grouped, we homogenize the eigenstrain inside each group, i.e., we assign the eigenstrain $\left(\varepsilon_n^{cen,t}, \varepsilon_n^{cen,b}\right)$ to all triangular elements that fall into the group n.

Consider N predefined peening regimes such as the ones illustrated in Fig. 7. Regime $i = 1, 2, ..., N$ induces expansions ε_i^t and ε_i^b on the treated and opposite layers, respectively. In addition, we consider the lack of treatment $\varepsilon_0^t = \varepsilon_0^b = 0$. Since the top and bottom surfaces can be peened independently, there are $(N+1)^2$ possible treatment combinations. Each treatment combination gives rise to a group centroid. Combining regime $i = 1, 2, ..., N$ on the top surface with regime $j = 1, 2, ..., N$ on the bottom surface leads to the following expansions of the top and

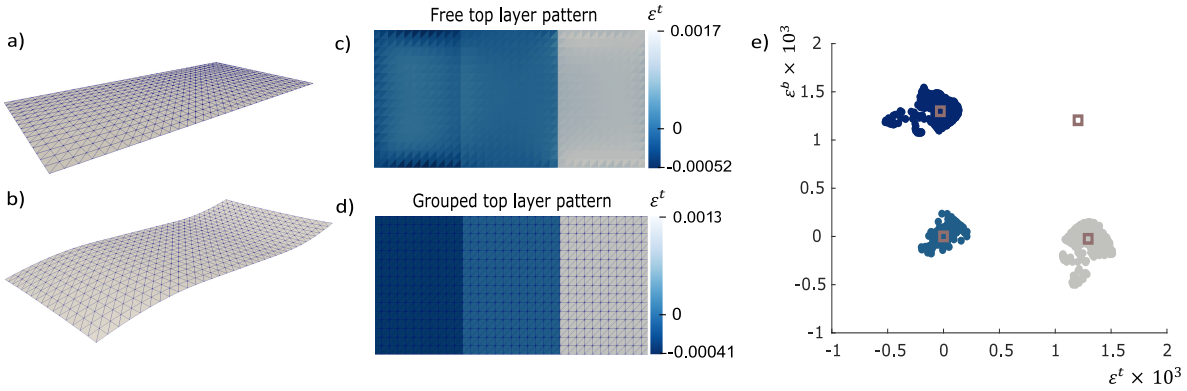

Fig. 6. Graphical representation of grouping of the eigenstrain pattern. The triangulated flat initial configuration (a) and the target configuration - wavy shape (b) - are the input data for the inverse problem resolution. We divide the eigenstrain pattern (c) into three zones treated uniformly (d). A plane with cartesian coordinates $(\varepsilon^t, \varepsilon^b)$ (e) illustrates the grouping from the numerical point of view. The colored points correspond to the eigenstrain assigned to each element of the triangular mesh. The four centroids are denoted by colored squares. They are generated by one peening regime and the lack of treatment as an additional regime. The grouping is based on calculation of the least Euclidean distance from the points to the group centroids. In the presented case there are no points close to the centroid denoting treatment from both sides, so the corresponding group is empty. Once the points are divided in groups, we homogenize the eigenstrain for all the elements attributed to the same group.

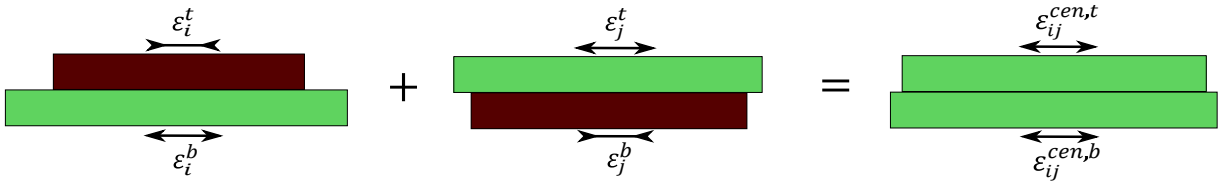

Fig. 7. Calculation of the group centroids. The group ij implies treatment from the bottom side with regime i and treatment from the top side with regime j. Its centroid is determined by a pair of parameters $\varepsilon_{ij}^{cen,t}$ and $\varepsilon_{ij}^{cen,b}$, and each of them is a superposition of eigenstrain generated by the two regimes that form this group: $\varepsilon_{ij}^{cen,t} = \varepsilon_i^t + \varepsilon_j^t, \varepsilon_{ij}^{cen,b} = \varepsilon_i^b + \varepsilon_j^b$. In this example, the regime i is more intense than the regime j, so $\varepsilon_{ij}^{cen,t} < \varepsilon_{ij}^{cen,b}$.

bottom surface: $(\varepsilon_i^t, \varepsilon_i^b) + (\varepsilon_j^t, \varepsilon_j^b) = (\varepsilon_{ij}^{cen,t}, \varepsilon_{ij}^{cen,b})$. Figure 7 illustrates this principle. Figure 6 e) also provides a cartesian representation of $(N+1)^2$ centroids for the case $N = 1$.

Numerical validation of the inverse problem solver

We generated target shapes numerically to test our algorithms for the iterative inverse problem resolution and grouping. To ensure that the target shapes were achievable with peen forming, we generated them by assigning a random peening pattern to the initial configuration and then solved the forward problem. The random peening patterns were generated following Alg. 2.

When the target shapes were generated, we solved the inverse problem for each of them

Algorithm 2 Generation of random peening patterns

```
Mark 1 to 6 random points on the top and bottom surfaces of the plate
for each point do
    Draw a square of random size (but not bigger than the plate size) centred on the point
    Assign randomly one of the available peening regimes to the square
    if the square protrudes beyond the plate area then
        Translate the part that protrudes symmetrically on the other side of the plate
    end if
    if the square superimposes with a previously drawn square on the same side then
        Erase the previously assigned regime in the superimposing area and leave only the
        latest one
    end if
end for
```

following Alg. 1 and then grouped the peening pattern. The predefined regimes were fixed as those that were originally used to generate the target shapes. To quantify the error, we solved the forward problem for the free and the grouped patterns. We thus obtained two final shapes for each testcase and compared them with the target shape by calculating the nondimensionalized Hausdorff distance Ω:

$$\Omega = \frac{d_H(\mathcal{C}_f, \mathcal{C}_{tar})}{\sqrt{A_{total}}}, \tag{34}$$

where $\mathcal{C}_f$ stands for the final configuration and $\mathcal{C}_{tar}$ stands for the target configuration. The overall process for the inverse problem validation is schematized in Fig. 8.

RESULTS

We generated 200 random patterns with Alg. 2 and applied them on a flat square plate (1×1 m). The plate thickness was arbitrarily assigned in each case and ranged from 2 mm to 15 mm. The Poisson's ratio was also arbitrarily picked between 0.32 and 0.36. The plate was meshed with 1152 triangular elements. The forward problem resolution took 10-30 seconds for one shape, depending

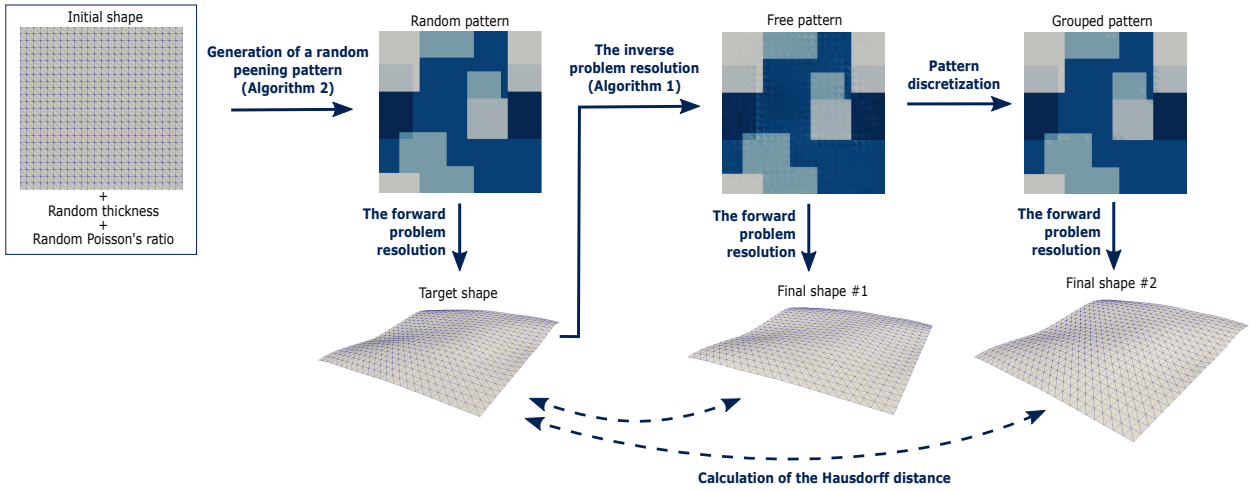

Fig. 8. A validation process to test the quality of the inverse problem resolution. The initial shape is fixed as a flat 1×1 m plate, its thickness and Poisson's ratio are chosen randomly. These parameters are kept constant throughout the whole validation process. A random peening pattern is generated following Alg. 2 and assigned to the initial shape. Different colors on the peening pattern correspond to different peening regimes applied from the top, bottom or both sides. We solve the forward problem taking the random pattern as input, and the result is used as the target shape for the inverse problem validation. The eigenstrain pattern is determined following Alg. 1 and grouped using pre-determined regimes. Finally, the forward problem is resolved for the free and the grouped patterns. The difference between the target shape and the two final shapes is quantified with the nondimensionalized Hausdorff distance Ω.

on the pattern and the plate thickness. Thus, the forward problem resolution took longer time for thinner plates with bigger treated areas due to larger deflection of these plates.

For the first 100 testcases (*series 1*), we made only one peening regime available, so the entire treated area was peened with the same parameters. For the second 100 testcases (*series 2*), we assigned randomly one of four available peening regimes to each square on both sides. We considered real peening regimes presented in [7]. The authors of this paper deduced idealized eigenstrain profiles from the residual stress measurements performed on the treated specimens. The idealized eigenstrain profiles were formulated as one uniformly expanding layer of a constant thickness. The layer thickness and the eigenstrain magnitude were different for each regime. We reformulated the idealized eigenstrain profiles in terms of $\left(\varepsilon^t, \varepsilon^b\right)$ by equating the total eigenstrain Γ and the first eigenstrain moment Γ_1 induced by $\left(\varepsilon^t, \varepsilon^b\right)$ and by the one expanding layer. Table 1 summarizes the eigenstrain $\left(\varepsilon^t, \varepsilon^b\right)$ induced by each of the four regimes applied on a 5 mm thick plate from the top side.

Figures 9 and 10 present the free and the grouped patterns along with the convergence curves

Table 1. The in-plane eigenstrain induced by the regimes used to generate the random peening patterns. The in-plane eigenstrain is presented for the case of a 5 mm thick plate. The peening regimes represent four real treatments inducing different eigenstrain profiles, which are examined in [7].

Regime	$\varepsilon^t \times 10^3$	$\varepsilon^b \times 10^3$
1	2.5	-0.4
2	3.2	-0.6
3	1.7	-0.4
4	2.0	-0.4

for two particular testcases from series 2: a low-error case and a high-error case. Figures 9 b) and 10 b) show that the free pattern on the final iteration is locally close to the originally generated random pattern. Due to that, most of the elements are grouped correctly, so that the eigenstrains prescribed by the grouped and the random patterns to these elements become equal (Fig. 9 c and Fig. 10 c). However, in each case there are elements that are attributed to a wrong group. In the low-error case this happens only for several elements. Consequently, the dimensionless error Ω is lower for the grouped pattern than for the free pattern. In the high-error case the grouped pattern undergoes the *checkerboard* problem, meaning that the pattern locally alternates two peening regimes over a certain area (Fig. 10 c). A large area affected by the checkerboard problem increases the Ω in comparison with the free pattern (Fig. 10 e). Nevertheless, the regimes that are mixed up in the checkerboard-affected zone have only a slight difference in terms of the induced eigenstrain, so the Ω increases up to 0.23% at most.

In terms of convergence, the most important correction is done on the first iteration after the initial guess, as illustrated by Fig. 9 e) and Fig. 10 e). Thus, the first iteration decreases the Ω by 65% on average, and the Ω becomes inferior to 0.1% for all the cases. All the subsequent iterations together decrease the Ω obtained on the first iteration by 60% on average. Because of the local nature of the eigenstrain adjustment, the solution does not converge to the exact target shape but to a shape which is close to the target. In other words, after several iterations the Ω plateaus at a low but finite level (Fig. 9 e and Fig. 10 e). The Ω may slightly grow during the subsequent iterations, but the stop criterion (26) terminates the iterative process as soon as this happens.

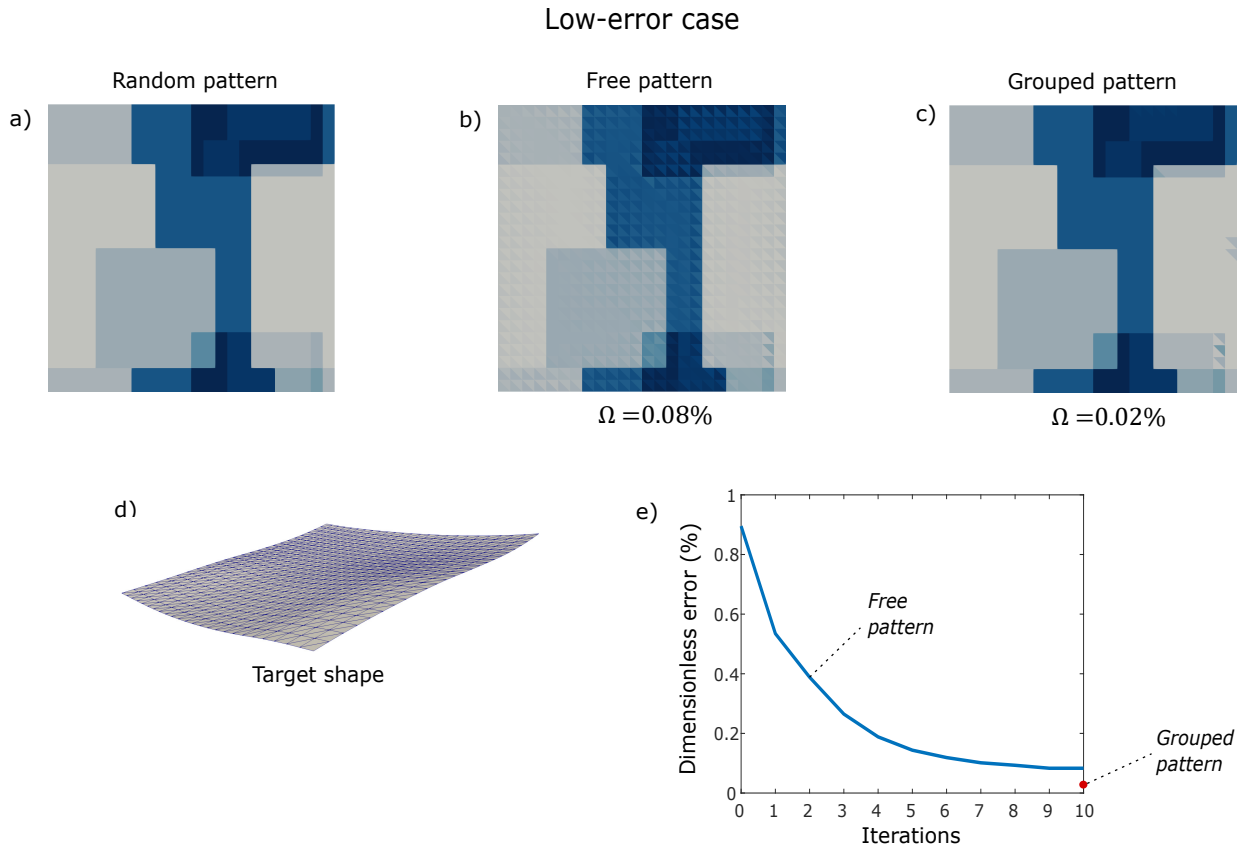

Fig. 9. One of the testcases from series 2 with low dimensionless error. The plate is 7 mm thick, and the Poisson's ratio equals 0.34. a) The random peening pattern generated for this testcase (top layer). Different colors on the peening pattern denote different peening regimes. b) The free peening pattern on the final iteration. c) The grouped peening pattern. A visual comparison of (c) and (a) shows that almost all elements were attributed to a correct group. Consequently, grouping decreased the dimensionless error Ω. d) The target shape induced by the pattern (a). The deformations are at their original scale. e) The convergence curve showing the dimensionless error Ω on each iteration. The optimization required 10 iterations, that was the maximum fixed for this test.

The results of the numerical validation are presented with histograms in Fig. 11. The inverse problem solver provided free peening patterns that led to the target shape with the Ω inferior to 0.35% for both series of tests (Fig. 11, top). The pattern optimization needed between 2 to 10 iterations, depending on the target shape.

The histograms in Fig. 11 show that the pattern grouping has decreased the Ω in most of the cases. Thus, the original pattern was perfectly reproduced for all testcases in series 1, so the Ω after grouping became less than $10^{-3}\%$. The corresponding Ω for series 2 was bigger because of the higher complexity of the grouping problem: four available regimes induced twenty-five group centroids for series 2, while there were only four centroids induced by one available regime for

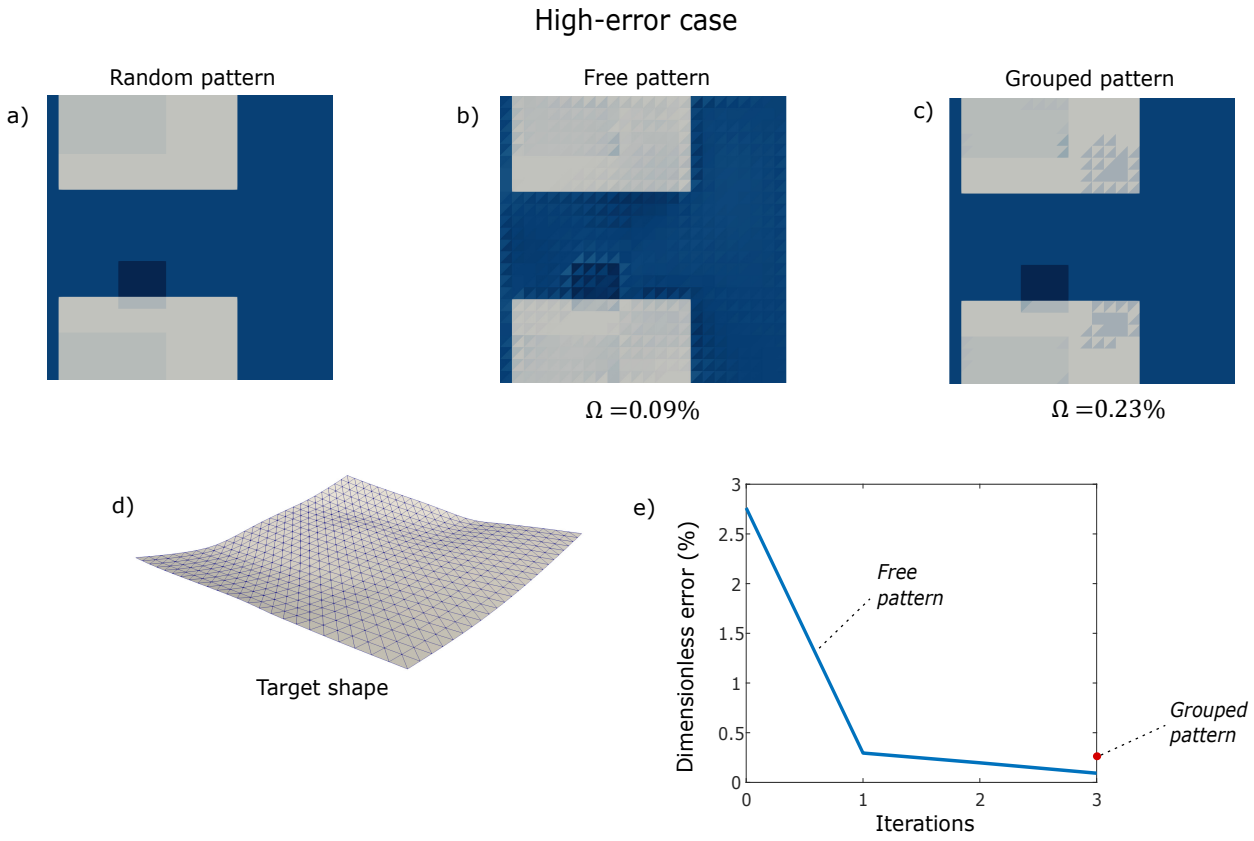

Fig. 10. One of the testcases from series 2 with high dimensionless error. The plate is 4 mm thick, and the Poisson's ratio equals 0.34. a) The random peening pattern generated for this testcase (top layer). Different colors on the peening pattern denote different peening regimes. b) The free peening pattern on the final iteration. c) The grouped peening pattern. A visual comparison of (c) and (a) indicates elements that were not attributed to a correct group. The deformations are at their original scale. However, grouping decreased the dimensionless error Ω in this case. d) The target shape induced by the pattern (a). e) The convergence curve showing the dimensionless error Ω on each iteration. The optimization required 3 iterations to converge.

series 1. The group centroids for series 2 were situated close to each other, so several testcases were significantly affected by the checkerboard problem, as illustrates Fig. 10 c). This explains the increased error after grouping for 18 cases out of 100 from series 2.

DISCUSSION

The described inverse problem resolution algorithm relies on the assumption that the peening treatment induces isotropic expansions. In practice, however, peen forming sometimes induces different eigenstrain along the x and y axes: $\varepsilon_{xx}(x,y,z) \neq \varepsilon_{yy}(x,y,z)$. Such anisotropic expansions are due to plastic anisotropy of the treated material, which is especially explicit for rolled

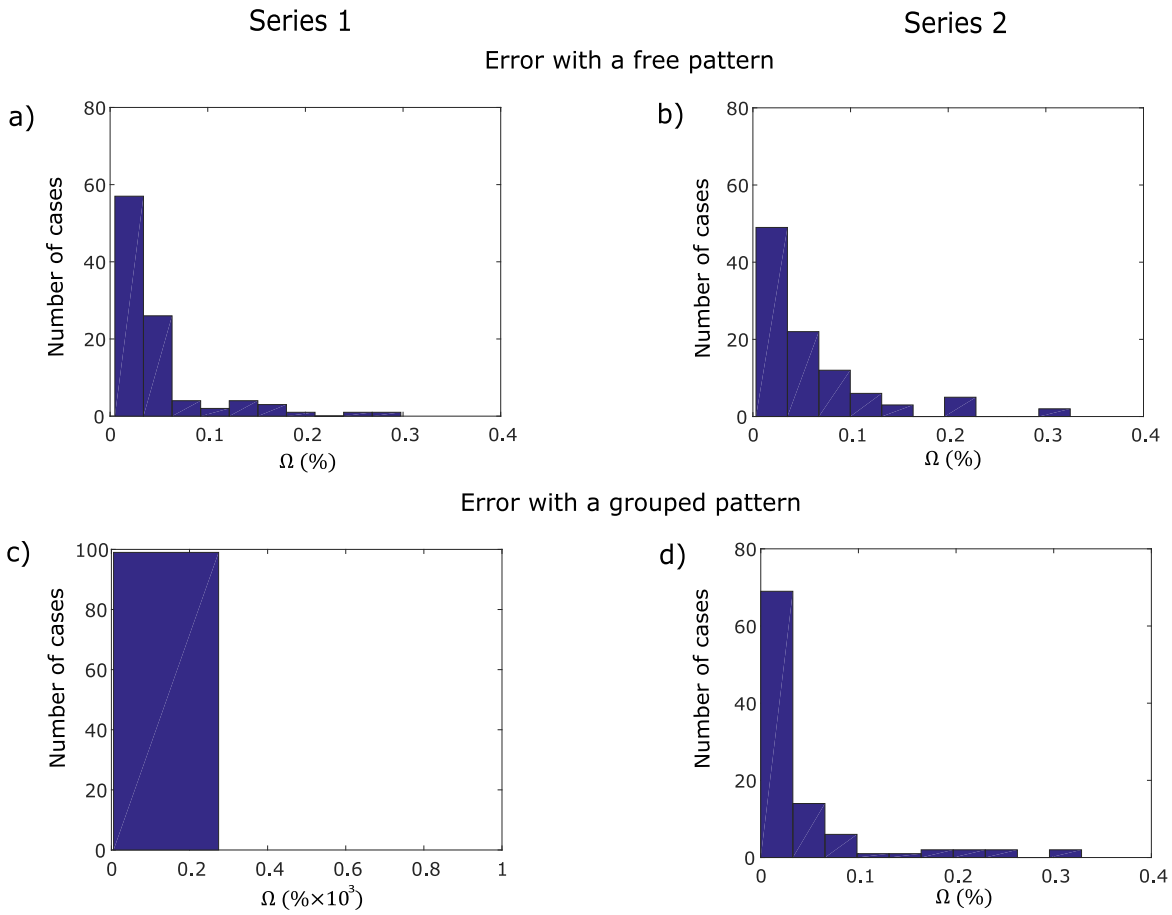

Fig. 11. Histograms evaluating the dimensionless error Ω between the target shapes and the final shapes obtained during the numerical validation of the inverse problem solver. All in all, 200 testcases were considered. They were divided in two series of 100 cases each. The target shapes in series 1 were obtained with one peening regime, and the same peening regime was fixed as the only available for the grouping stage. The target shapes in series 2 were obtained with four different peening regimes, and the four predefined regimes were available for grouping. Figures (a) and (b) show the dimensionless error induced by application of the free pattern for series 1 and 2 correspondingly. Similarly, figures (c) and (d) represent the dimensionless error induced by the grouped pattern.

aluminum sheets, and to prestressing the component in one direction before treatment, i.e., stress peen forming. This effect is examined in detail in [31]. For uniform plastic anisotropy which does not vary over the area of the plate, the inverse problem resolution algorithm can be easily adapted by introducing a fixed eigenstrain anisotropy coefficient χ in the model:

$$\varepsilon^j_{xx} = \frac{(1+\chi)}{(1-\chi)}\varepsilon^j_{yy}, \quad \text{for} \quad j = t, b. \tag{35}$$

This relation may be imposed after adjustment of the bilayer rest fundamental forms $\mathbf{a}_{r,t}$ and $\mathbf{a}_{r,b}$ on each iteration. Thus, the forward problem will be solved taking into account the plastic anisotropy.

Given that the rest fundamental forms are numerically adjusted for each triangular element separately, the efficiency of the inverse problem resolution depends on the consistency between the target mesh and the initial mesh. More precisely, it depends on the mapping $\vec{m}$ between the initial 2D shape and the target 3D shape. The general requirement for the mapping is to preserve the shape of each triangular element as well as possible. This minimizes the local eigenstrain assigned by the algorithm and makes the computed free pattern smoother. This problem was not faced during the numerical validation because the target shapes were derived from the initial shapes through the forward problem resolution, so they were optimally meshed by default.

The mesh consistency can be ensured by fixing the target shape mesh and by its mapping onto the initial 2D geometry. The fixed initial geometry is an important constraint for the mapping because it involves a fixed 2D boundary. The mapping can be done using the methods oriented on maximal preservation of local angles, such as the Least Squares Conformal Mapping (LSCM) algorithm [32]. Next, local mesh distortions with respect to the target mesh can be minimized using a numerical optimization algorithm. For example, the L-BFGS algorithm that we use for the global elastic energy minimization can cope with this task.

CONCLUSION

The theory of non-Euclidean plates in combination with the eigenstrain approach provides an extensive theoretical framework for the modeling of shot peen forming. The eigenstrain approach represents the treated plate as a bilayer undergoing nonuniform eigenstrain, and the theory of non-Euclidean plates accurately solves the forward problem for this case. The deformed shape is calculated through minimization of the global elastic energy following analytical gradients.

The iterative inverse problem resolution is based on the comparison of geometrical properties of the plate in its current and target configurations. The adjustment of the prescribed eigenstrain on each iteration is done on a local scale involving simple arithmetic operations and takes negligible amount of time. A low number of iterations (not more than 10) ensures fast resolution of the inverse

problem. The eigenstrain formulation of the inverse problem makes the algorithm applicable for any type of processes that induce small isotropic eigenstrain. These include, among others, laser peen forming of metal plates or 4D printing of shape-shifting polymer structures. The precision of the inverse problem resolution is independent of plate thickness and its mechanical properties. It is, however, dependent on consistency between the initial and the target meshes.

The pattern grouping makes the inverse problem solution practically applicable. It adds uncertainty to the solution, but in many cases it decreases the induced error. The grouping algorithm can locally mix up the peening regimes having slightly different intensities. A method for correction of the local grouping errors would enhance the solution quality.

The future work implies experimental validation of the proposed inverse problem simulation technique. It will reveal practical constraints that may cause simulation error. Among others, we will examine influence of the peening parameters and of the material plastic anisotropy on the induced eigenstrain.

ACKNOWLEDGEMENTS

The authors gratefully acknowledge financial support from The Fonds de recherche du Québec – Nature et technologies (FRQNT) and The Aluminium Research Center (REGAL).

REFERENCES

[1] Ramati, S., Kennerknecht, S., and Levas-Seur, G., 1999. “Single piece wing skin utilization via advanced peen forming technologies”. *Proceedings of the ICSP7, Warsaw*.

[2] De los Rios, E., Walley, A., Milan, M., and Hammersley, G., 1995. “Fatigue crack initiation and propagation on shot-peened surfaces in a316 stainless steel”. *International Journal of Fatigue,* **17**(7), pp. 493–499.

[3] Faucheux, P. A., 2019. “Simulating shot peen forming with eigenstrains”. PhD thesis, Polytechnique Montreal, December.

[4] Chen, Z., Yang, F., and Meguid, S., 2014. “Realistic finite element simulations of arc-height

development in shot-peened almen strips". *Journal of Engineering Materials and Technology,* **136**(4).

[5] Mura, T., 2013. *Micromechanics of defects in solids*. Springer Science & Business Media.

[6] Korsunsky, A., 2005. "The modelling of residual stresses due to surface peening using eigenstrain distributions". *The Journal of Strain Analysis for Engineering Design,* **40**(8), pp. 817–824.

[7] Faucheux, P. A., Gosselin, F. P., and Lévesque, M., 2018. "Simulating shot peen forming with eigenstrains". *Journal of Materials Processing Technology,* **254**, pp. 135–144.

[8] Siguerdidjane, W., Khameneifar, F., and Gosselin, F. P., 2020. "Efficient planning of peen-forming patterns via artificial neural networks". *Manufacturing Letters,* **25**, pp. 70–74.

[9] Pajot, J. M., Maute, K., Zhang, Y., and Dunn, M. L., 2006. "Design of patterned multilayer films with eigenstrains by topology optimization". *International journal of solids and structures,* **43**(6), pp. 1832–1853.

[10] Miao, H. Y., Levesque, M., and Gosselin, F., 2021. Shot peen forming pattern optimization to achieve complex target shapes: the inverse problem, Apr.

[11] Luo, M., Hu, Y., Hu, L., and Yao, Z., 2020. "Efficient process planning of laser peen forming for complex shaping with distributed eigen-moment". *Journal of Materials Processing Technology,* **279**, p. 116588.

[12] Efrati, E., Sharon, E., and Kupferman, R., 2009. "Elastic theory of unconstrained non-euclidean plates". *Journal of the Mechanics and Physics of Solids,* **57**(4), pp. 762–775.

[13] Efrati, E., Sharon, E., and Kupferman, R., 2013. "The metric description of elasticity in residually stressed soft materials". *Soft Matter,* **9**(34), pp. 8187–8197.

[14] Pezzulla, M., Shillig, S. A., Nardinocchi, P., and Holmes, D. P., 2015. "Morphing of geometric composites via residual swelling". *Soft Matter,* **11**(29), pp. 5812–5820.

[15] Pezzulla, M., Smith, G. P., Nardinocchi, P., and Holmes, D. P., 2016. "Geometry and mechanics of thin growing bilayers". *Soft matter,* **12**(19), pp. 4435–4442.

[16] Chen, H.-Y., Sastry, A., van Rees, W. M., and Vouga, E., 2018. "Physical simulation of environmentally induced thin shell deformation". *ACM Transactions on Graphics (TOG),* **37**(4),

pp. 1–13.

[17] van Rees, W. M., Matsumoto, E. A., Gladman, A. S., Lewis, J. A., and Mahadevan, L., 2018. "Mechanics of biomimetic 4d printed structures". *Soft Matter,* **14**, pp. 8771–8779.

[18] Aharoni, H., Xia, Y., Zhang, X., Kamien, R. D., and Yang, S., 2018. "Universal inverse design of surfaces with thin nematic elastomer sheets". *Proceedings of the National Academy of Sciences,* **115**(28), pp. 7206–7211.

[19] van Rees, W. M., Vouga, E., and Mahadevan, L., 2017. "Growth patterns for shape-shifting elastic bilayers". *Proceedings of the National Academy of Sciences,* **114**(44), pp. 11597–11602.

[20] Klotz, T., Delbergue, D., Bocher, P., Lévesque, M., and Brochu, M., 2018. "Surface characteristics and fatigue behavior of shot peened inconel 718". *International Journal of Fatigue,* **110**, pp. 10–21.

[21] Rossini, N., Dassisti, M., Benyounis, K., and Olabi, A.-G., 2012. "Methods of measuring residual stresses in components". *Materials & Design,* **35**, pp. 572–588.

[22] Flavenot, J. F., and Niku-Lari, A., 1977. La mesure des contraintes résiduelles. Méthode de la flèche. Méthode de la source des contraintes. Application au grenaillage de précontrainte et à d'autres traitements superficiels. Tech. Rep. 31, CETIM, Senlis, France, Sept.

[23] Prime, M. B., and Hill, M. R., 2002. "Residual stress, stress relief, and inhomogeneity in aluminum plate". *Scripta Materialia,* **46**(1), pp. 77–82.

[24] Korsunsky, A., 2006. "Residual elastic strain due to laser shock peening: modelling by eigenstrain distribution". *The Journal of Strain Analysis for Engineering Design,* **41**(3), pp. 195–204.

[25] Ciarlet, P. G., 2005. "An introduction to differential geometry with applications to elasticity". *Journal of Elasticity,* **78**(1), pp. 1–215.

[26] Spivak, M., 1975. *A comprehensive introduction to differential geometry*, Vol. 3. Boston: Publish or Perish.

[27] Weischedel, C., Tuganov, A., Hermansson, T., Linn, J., and Wardetzky, M., 2012. "Construction of discrete shell models by geometric finite differences". Fraunhofer ITWM, Kaiserslautern, Germany.

[28] Liu, D. C., and Nocedal, J., 1989. “On the limited memory bfgs method for large scale optimization”. *Mathematical programming,* **45**(1), pp. 503–528.

[29] Tamstorf, R., and Grinspun, E., 2013. “Discrete bending forces and their jacobians”. *Graphical models,* **75**(6), pp. 362–370.

[30] van Rees, W. M., 2018. Code accompanying the 2018 soft matter paper "mechanics of biomimetic 4d printed structures". `https://github.com/wimvanrees/growth_SM2018`.

[31] Miao, H. Y., Faucheux, P. A., levesque, M., and Gosselin, F., 2021. Residual stress measurements of conventional and stress peen formed 2024-t3 aluminum sheets, Apr.

[32] Lévy, B., Petitjean, S., Ray, N., and Maillot, J., 2002. “Least squares conformal maps for automatic texture atlas generation”. *ACM transactions on graphics (TOG),* **21**(3), pp. 362–371.

LIST OF FIGURES

LIST OF TABLES